DISTINGUISHING ERUPTIVE UNITS ON THE SOUTHERN EAST PACIFIC RISE USING GEOMAGNETIC PALEOINTENSITY AND GEOCHEMISTRY

by

Vera Soltes

A Thesis Submitted in

Partial Fulfillment of the

Requirements for the Degree of

Master of Science

in Geosciences

at

The University of Wisconsin-Milwaukee

August 2025

ABSTRACT

DISTINGUISHING ERUPTIVE UNITS ON THE SOUTHERN EAST PACIFIC RISE USING GEOMAGNETIC PALEOINTENSITY AND GEOCHEMISTRY

by

Vera Soltes

The University of Wisconsin-Milwaukee, 2025
Under the Supervision of Professor Julie Bowles

The size and frequency of mid-ocean ridge eruptions are important variables in understanding ocean crustal accretion, but are poorly understood. Young flows are difficult to date because recurrence intervals are typically shorter than the resolution of most radiometric dating systems. We attempt to differentiate eruptive units at 17°-19°S on the superfast spreading southern East Pacific Rise (SEPR), by combining geochemical data with geomagnetic paleointensity of submarine basaltic glass (SBG) specimens to assess inter- and intra-flow variability through a joint cluster analysis. At the SEPR, geochemistry alone is not necessarily indicative of distinct eruptive events. Paleointensity allows us to add a temporal constraint, as field intensity is recorded at the time of eruption.

Samples were collected during *Alvin* and *Nautile* dives where direct observations enabled relative age assessments (Sinton et al., 2002). Specimens were chosen from known flow fields to contrast with data across contacts and within the identified flow. These known flow classifications allow us to evaluate the natural scatter in a single eruptive event and to test the cluster approach. Each flow was represented by 2 to 15 samples, but a statistical analysis indicates these numbers are insufficient to differentiate most flows based on paleointensity

alone. The cluster analysis models four data clusters interpreted to represent distinct flow units in the 17°26’S region and seven clusters around 18°38’S. Clusters generally align with prior flow observations, and incongruities could indicate a newly identified flow or a lack of samples needed to provide statistical distinction. The addition of geochemistry can differentiate flows with non-statistically distinct paleointensity means. However, if both geochemistry and paleointensity are similar, a larger sample size would be required to differentiate flows.

In addition to identifying the number and size of eruptive clusters, global magnetic field models evaluated at the SEPR allow us to estimate absolute ages for defined flows based on paleointensity. Paleointensity estimates range from 28-43 μT at flows surrounding 17°26’S and 30-48 μT at flows surrounding 18°38’S. Estimated ages for 17°26’S flows place eruptions between 1887-2016. Estimated dates for 18°38’S eruptions are between 1890-1920. Once flows were defined, absolute ages from paleointensity determined recurrence intervals at 17°26’S to be ~100 years and intervals at 18°38’S to be a few decades.

Ref: Sinton et al. (2002), *J. Geophys. Res*., 107, 1-21, doi: 0.1029/2000JB000090.

TABLE OF CONTENTS

LIST OF FIGURES

LIST OF TABLES

ACKNOWLEDGEMENTS

My gratitude to the UWM Geosciences Department, the UWM Paleomag Lab and all the cats I met along the way. This work was supported by the National Science Foundation grant #2128108 to J Bowles. Special thanks to John Sinton for providing the glass specimens.

Introduction

Mid-ocean ridge processes are reflected in the size, shape, and eruptive frequency of submarine lava flows, but dating and differentiating very young flows (< ~1000 years) remains challenging (Bowles et al., 2014). At a 25°N segment of the slow-spreading Mid-Atlantic Ridge, an observed recurrence interval is ~5-10 thousand years (Cann et al., 2005). The Reykjanes Peninsula, a hotspot-influenced segment of the Mid-Atlantic Ridge above sea level, is characterized by ~800-year repose periods between eruptive episodes. An eruption in 2021 marked the beginning of a new episode, followed by 8 eruptions in the past 3 years (Troll et al., 2024). Mid-ocean ridge lavas from a fast-spreading environment are thought to have eruption recurrence intervals of years to tens of years. Due to these short intervals and large magma chambers, eruptions can occur faster than the magma chamber source changes (Sinton et al., 2002). As a result, separate flows could have an identical geochemistry. On the other hand, a differentiated magma chamber could cause a single flow to have a high geochemical variability due to variability in the source. Sediment cover observations can also be used to differentiate older (more sediment) from younger flows (less sediment), but flow morphology and currents also affect the amount of sediment cover, so the relationship isn't necessarily direct. Geomagnetic paleointensity can provide limited absolute age estimates and can act as a temporal constraint on some of the relative dating methods (Carlut et al., 2004; Bowles et al., 2005, 2014).

Geomagnetic paleointensity recorded by submarine basaltic glass (SBG) can be combined with geomagnetic field strength models going back several thousand years (e.g., Constable et al., 2016; Jackson et al., 2000) to determine absolute eruptive ages for mid-ocean ridge lavas from a fast-spreading environment. Earth generates its own magnetic field due to convection in the liquid outer core, the strength of which can be recorded by magnetic minerals (e.g. magnetite) in glass from lava flows when they erupt and cool. The magnetization of these magnetic minerals today is proportional to field strength at the time of emplacement which can be referenced against known variations in Earth's magnetic field to constrain absolute or relative ages. Due to the monotonically decreasing field intensity over the last ~400 years, absolute age constraints can be determined for younger lavas within this time frame. For older lavas, paleointensities do not provide unique emplacement dates but can provide relative age estimates (Figure 1).

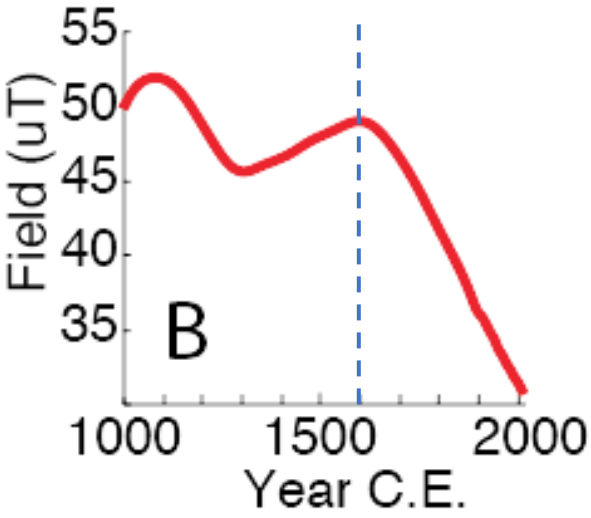

Figure 1: Geomagnetic field intensity variation over the last 1000 years at 19°S, SEPR (evaluated models of Constable et al. [2016] and Jackson et al. [2000]). Dotted line indicates when the field began monotonically decreasing.

Study Objectives

The objectives of this study are twofold: 1) Assess the use of a joint paleointensity-geochemistry cluster analysis to define eruptive events; and 2) quantify within-flow paleointensity variability at two locations along the SEPR.

Combining paleointensity and geochemistry could provide a way to better distinguish between separate flows. Using either parameter alone is problematic as inter- and intra-flow variations in both are not reliably different. Two flows could have similar compositions but different paleointensities indicating separate eruptions. This is particularly applicable on the SEPR as fast-spreading rates commonly result in eruption recurrence intervals shorter than the time it takes for the magma chamber composition to change (Sinton et al., 2002). Conversely flows could have different compositions but similar paleointensities, perhaps indicating eruptions occurring at the same time but drawing upon different magma sources (e.g., Bowles et al., 2005). Composition can even vary within a single flow due to a fractionated magma chamber (Goss et al., 2010). The proposed cluster analysis uses the paleointensity and geochemical data to define eruptive clusters where data within a cluster represents a single eruption or series of eruptions within a short period of time.

Using paleointensity to define eruptive clusters requires understanding of the natural variability in paleointensity within a single flow. Different paleointensities could be caused by intra-flow variability or could represent different emplacement ages and thus, different eruptive events. Should paleointensities within a single flow be more similar to each other than to paleointensities from a different flow, it would suggest paleointensity to be an accurate method of differentiating separate flows. The ability to make this distinction likely depends on how much time has passed between the two eruptive events. The more different the paleointensity, the easier it will be to distinguish the flows.

Measured paleointensities within a single flow can vary due to local magnetic anomalies caused by existing magnetic topography which can bias mean paleointensities and/or introduce scatter. Such an effect would be regionally dependent as different sites have different underlying

topography (Bowles et al., 2014). In flatter areas and regions with north-south trending structures, local magnetic anomalies are less impactful. Variations in the natural cooling rate could also introduce scatter. In certain grains, a slower cooling rate can result in greater magnetization acquisition (Dodson and McLelland-Brown, 1980; Halgedahl et al., 1980).

I will be combining new paleomagnetic data with existing geochemical data to assess the paleointensity scatter within flows that have already been mapped (Sinton et al., 2002).(Sinton et al., 2002). Combining paleomagnetic data with geochemical data will inform how many samples are required to adequately characterize a flow. Additionally, I will determine if paleointensity combined with geochemistry can uniquely identify individual flows. I will use a formal cluster analysis to see if individual flows cluster more tightly when using the combined data set as opposed to the data sets individually. If we can show this method works on flows that are already well-mapped, then we can extend the approach to areas where flow boundaries are poorly defined.

Background

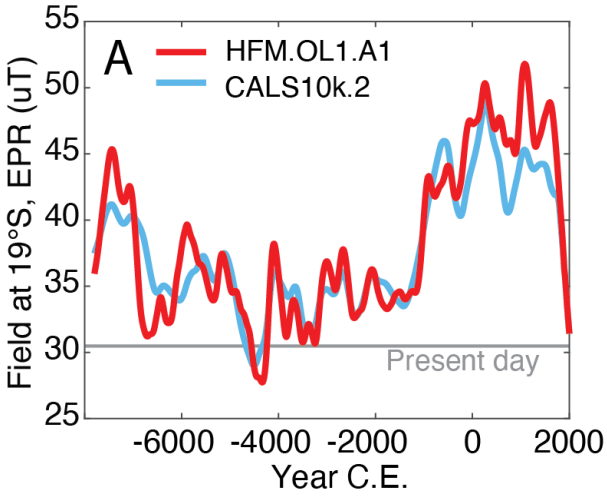

Figure 2: Geomagnetic field intensity variation on the southern East Pacific Rise according to Constable et. al., 2016 constrained to agree with records over the past 400 years (Jackson et. al., 2000).

Magnetization

The magnetization of a lava flow is proportional to the strength of the field at the time of eruption (paleointensity). The magnetization measured before lab experimentation is the natural remanent magnetization (NRM) and is important to determine the original conditions under which the rock formed. Thermal remanent

magnetization (TRM) is a magnetization acquired by cooling specimens from above their Curie temperature through their blocking temperature in the presence of a magnetic field. Above the Curie temperature, a material will not show ordered ferromagnetic behavior—magnetic behavior even in the absence of a field. Below the Curie temperature but above the blocking temperature, a material will display ferromagnetic behavior, but the direction of magnetization will change to align with a changing field. Below the Curie and blocking temperature, a material will behave ferromagnetically, but the magnetization direction will not change to align with a weak, Earth-like changing field. It will retain the magnetization direction it had when cooled below the blocking temperature.

Magnetization is fundamentally derived from unpaired electron spins within the crystal structure and is affected by the balance between thermal and magnetic energies in the grains (Tauxe et al., 2018). Above the Curie temperature thermal energy dominates, randomizing electron spins and resulting in a net zero magnetization overall. Below the Curie temperature, exchange energy becomes more important allowing for ferromagnetic behavior to occur and the magnetization direction to align with the current field. Exchange energy is the energy generated by neighboring electron spins interacting with each other and is minimized when the spins are parallel or antiparallel, depending on the crystal structure. Cooling beneath the blocking temperature allows for magnetic anisotropy energy to lock the direction of the magnetic moment. Magnetic anisotropy energy is the energy required to flip the moment from one easy axis to another. This energy is typically dependent on the shape of the grain (Tauxe et al., 2018). Different minerals will have different crystal structures and/or different grain shapes resulting in variable Curie and blocking temperatures for different minerals.

Additional magnetic properties of a mineral depend on its domain state—which is related to grain size. The specific dimensions are mineral-dependent; however, the domain states from smallest to largest are superparamagnetic, single domain, vortex (pseudo-single domain), and multi-domain. Single domain (SD) grains exhibit a stable, uniform magnetization throughout the entire grain (Tauxe et. al., 2018). The behavior of SD grains is easily predicted by Néel theory (Néel, 1949), and these types of grains behave ideally in experiments designed to recover paleointensity. Submarine basaltic glass typically contains single domain low-Ti titanomagnetite grains, as the quick cooling prevents the grains from growing to a vortex or multi-domain size (Pick and Tauxe, 1993; Zhou et al., 2000; Carlut and Kent, 2000; Bowles et al., 2011). Smaller superparamagnetic grains are also present but are not ideal as their magnetization is unstable over very short time scales and thus, do not contribute to the magnetic moment.

Paleointensity

The upper limit for the average recurrence interval of axial lavas from a fast-spreading environment has been estimated to be ~200 years (Gee et al., 2000; Carlut and Kent, 2000; Bowles et al., 2005, 2006). Because field strength increases and decreases throughout time (Figure 2), lavas believed to be older than ~400 years cannot be uniquely dated using paleointensity; however, relative ages are important for differentiation purposes. If two flows have different paleointensities, then they are not the same age even if their chemical composition is similar. Likewise, two flows with similar paleointensities and different compositions could indicate similar ages and different magmatic processes or sources.

Paleointenisty is the strength of the Earth's magnetic field at a specific point in time. For weak magnetic fields (such as Earth's), the relationship between applied field and resulting magnetization is typically linear (Tauxe and Yamazaki, 2015) such that:

$$M_{NRM} \approx \alpha_{anc} H_{anc}$$

and

$$M_{lab} \approx \alpha_{lab} H_{lab}$$

where α is a proportionality constant that relates the magnetization (M) to the field it was acquired in ($H_{anc,}$ the ancient field, or H_{lab}, the laboratory field).

By applying a known laboratory field (H_{lab}) and measuring the resulting magnetization (M_{lab}), we can find the proportionality constant. Assuming the laboratory constant (α_{lab}) is equivalent to the original constant (α_{anc}) allows us to determine the ancient field (H_{anc}, paleointensity) that resulted in the magnetization at the time the rock formed (M_{NRM}). Rearranging the prior equations:

$$H_{anc} = \frac{M_{NRM}}{M_{lab}} H_{lab}$$

In practice, the proportionality constant is derived from the ratio of the NRM to a laboratory-induced TRM, where it is assumed that the NRM is thermal in nature and acquired when the lava flow erupted and cooled.

In a Thellier-type (Thellier and Thellier, 1959) paleointensity experiment, stepwise heating gradually replaces NRM with a laboratory TRM to isolate the most stable magnetization assumed to correspond with emplacement. For a given temperature, the specimens are heated in alternating zero-field steps to remove NRM and in-field steps to acquire partial TRM (pTRM). pTRM gained at that temperature is calculated by vector subtraction between the in-field and zero-field steps. The results are plotted on an Arai plot (Nagata et al., 1963) (Figure 3) of NRM remaining vs. pTRM gained. At regular intervals, an in-field magnetization step is repeated at a previous temperature to check if the experimental heating has altered the magnetic minerals in the glass (Coe, 1967). If the so-called pTRM check plots on the same trend, then the specimen is presumed to be unaltered. If it does not, then chemical changes to the magnetic mineralogy mean that magnetizing capacity of the specimen has changed and is no longer representative of emplacement conditions.

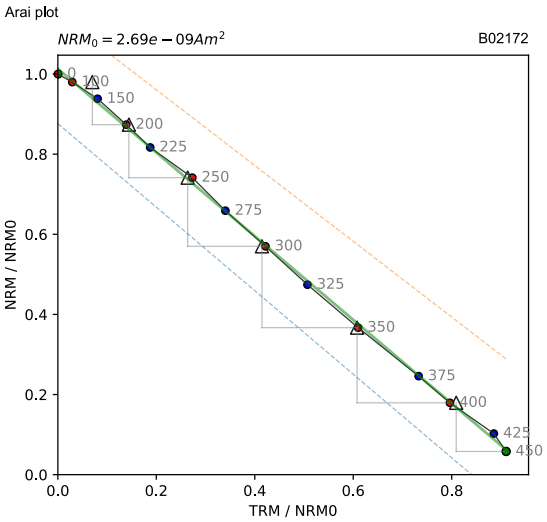

Figure 3: Arai plot for specimen B02172 of NRM remaining (y-axis) vs. pTRM gained (x-axis). Both axes are normalized by the starting NRM. Backcheck (triangle) performed every other temperature step.

Geochemistry

The chemical composition of individual lava flows reflects the structure of magma chamber associated with that flow (e.g., size, temperature, composition) and is reliant on supply, storage, and mode of magma transport (Sinton et al., 2002; Goss et al., 2010). The composition of a single lava flow is not necessarily homogenous. Generally, compositional heterogeneity within a single flow is higher with higher eruption volume; however faster spreading rates tend to produce lower compositional heterogeneity within a single flow (Rubin et al., 2001). For example, the North Cleft sheet flow on the medium-spreading rate Juan de Fuca ridge has a volume of 10.5 x 10^6 m^3 and is moderately heterogeneous while the Animal Farm flow on the superfast-spreading SEPR has a volume of ~220 x 10^6 m^3 and a compositional variation only slightly higher than analytical uncertainty (Rubin et al., 2001; Sinton et al., 2002).

Higher homogeneity indicates a more stable magma chamber with possibly high eruptions rates. Along the EPR, the $TiFe_x$ (Ti and Fe concentrations corrected for crystal fractionation [e.g., Waters et al., 2013]) variability within a single flow can be equal to variability between different flows. Thus, mapping flow boundaries with compositional data alone produces ambiguous results (Rubin et al., 2001).

Perhaps an intuitive understanding is that eruptions occurring close together in time would have a similar geochemistry since the composition of the magma chamber would not have had enough time to change. Likewise, lava flows with differing geochemistry could indicate drastically different eruption times which would have allowed the magma chamber composition to change over time. If the difference in geochemistry is due to the evolution of the magma chamber, then flows with different compositions should indicate separate eruptive events.

Axial Seamount on the Juan de Fuca Ridge has a well-developed eruption chronology and has seen several distinct stages of lava composition. Over the last 1000 years, Axial Seamount lavas have primarily been of two types: aphyric transitional MORB with MgO wt% $\leq$7.9% and phyric to ultraphyric normal MORB with MgO wt% $>$7.9%. The first type was prominent before 1100 before transitioning to the second type from 1220 to 1300 (Chadwick et al., 2016). 1600 marked a return to the first type until high- MgO flows on Axial Seamount in 2015 showed the most mafic lavas to have erupted in the region since ~1450 (Clague et al., 2013). These higher-temperature flows have the transitional MORB composition like the first type but higher MgO wt% and phyric textures like the second type indicating new magma from the mantle driving a geochemical change in the resultant flow. Axial Seamount is partially supplied by the Cobb hotspot, so it may not be a perfect analogy for a typical mid-ocean ridge setting (Chadwick et al., 2016).

Unfortunately, geochemical variability alone can't provide absolute flow boundaries as variations can also occur within a flow from a single eruptive event. For instance, flows from the 2005-2006 eruptions on 9°46'-9°56'N displayed variation in MgO wt% higher than analytical uncertainty, likely related to short-term magma chamber evolution (Goss et al., 2010). Lavas in the central area have the highest MgO wt% overall at 8.0-8.5%. One group of southern lavas show a similar composition while another has MgO less than 8.0 wt%. Northern lavas have MgO wt % in between central and southern contents. Geochemistry of the northern lavas point to crystal fractionation while similarities of primitive central and southern lavas indicate additional magma mixing driving variability (Goss et al., 2010).

Southern East Pacific Rise

Paleointensity methods have been successfully applied in investigating cycles of volcanic activity predominantly along the northern East Pacific Rise (Bowles et al., 2006) and Galapagos Spreading Center (Bowles et al., 2014) but limited paleointensity data exist on the southern East Pacific Rise (SEPR) (Carlut and Kent, 2000; Gee et al., 2000; Bowles et al., 2005). Dive observations can help identify the boundaries of individual eruptive episodes comprised of periods of closely spaced eruptions or "flows" (Sinton et al., 2002). These boundaries outline areas that will be referred to as "flow fields." The shorter the recurrence interval, the more ambiguous the distinction between "flows" and "flow fields" becomes. Refining the usage of a paleointenisty and geochemistry cluster analysis in areas with already defined flow fields could allow for applications in sites with fewer data, such as on the SEPR.

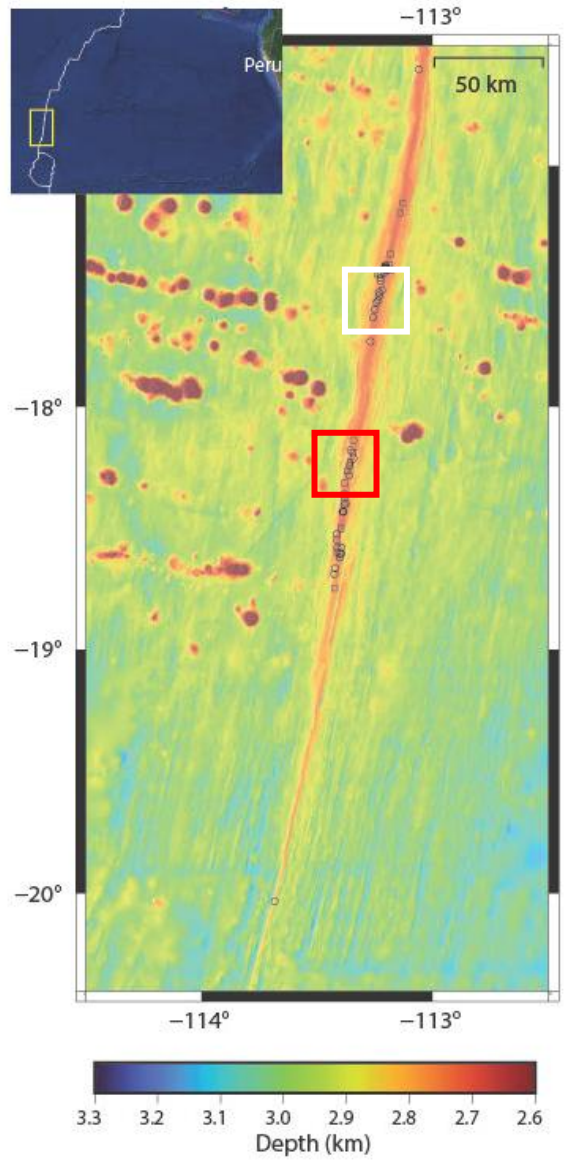

Figure 4: A) Location of SEPR 17°-19°S segment. B) SEPR study site locations: 17°S flow field (white) and 18°S flow field (red). Small circles (squares) are Alvin (Nautile) dive locations.

This project analyzes geomagnetic paleointensity in submarine basaltic glass specimens from the SEPR to assess the within-flow field variability in paleointensity and test the use of a joint cluster analysis as a tool to identify discrete flow fields. Individual eruptions on the superfast-spreading (141-162 mm/yr) (Cormier and Macdonald, 1994) SEPR are

characterized by low erupted magma volumes and high effusion rates, suggesting this is an area of frequent and short-lived eruptions (Sinton et al., 2002). Three regions between 17°-18°S have already been mapped via submersible (Figure 4), and some flow field boundaries were identified (Sinton et al., 2002). The limited existing paleointensity data suggest that at least 5 flow fields were emplaced within the past 400 years (Carlut and Kent, 2000; Bowles et al., 2005). This project aims to quantify the amount of natural variability within a single flow field and combine paleointensity and geochemistry to better delineate discrete episodes of SEPR eruptive activity.

Two types of segments have been distinguished in the region (Auzende et al., 1996): volcanically dominated and tectonically dominated. Volcanically dominated segments are characterized by prominent axial domes and fresh lava flows. Tectonically dominated segments are characterized by fracture and fissure systems and a developing axial graben (Auzende et al., 1996). The two flow fields of interest at 17°S and 18°S are volcanically dominated segments (Sinton et al., 2002).

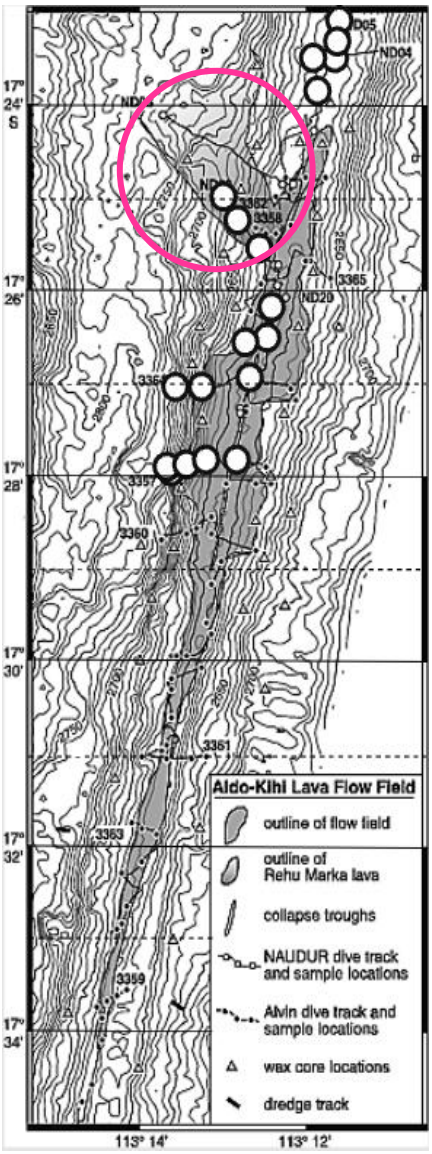

Figure 5: Dives at 17°S flow fields on the SEPR. White circles are sampling sites selected for this study. Most samples were selected within the Aldo-Kihi flow field; however, some were intentionally selected to be outside the flow field (modified from Sinton et al., 2002). Pink circle denotes Rehu Marka location.

17°S

The region between 17°24'S and 17°34'S contains at least two mapped flow fields younger than the surrounding areas. Active hydrothermal sites were observed around 17°25'S indicating relatively recent volcanic activity around the Aldo-Kihi and Rehu Marka flow fields. Sites were located on large flows characterized by shimmering water, lack of chimneys, and motile animals. The shimmering water is likely due to heating of seawater by recent volcanic activity. Recent eruptions also mean sessile animals would not have had enough time to settle in the area (Auzende et al., 1996).

The Aldo-Kihi flow field (Figure 5) is primarily unsedimented lobate flows, although lava channels often contain jumbled sheet flows. Some lavas are slightly less sedimented than surrounding lavas. In some areas, glassy pillows overlay lobate flows covered in hydrothermal sediment. Aldo-Kihi is likely comprised of multiple individual lava flows as dive observations identified different degrees of sediment cover within the flow field. Mappable age contrasts as determined by sediment cover between Aldo-Kihi and older flow fields, such as the Rehu Marka, suggest Aldo-Kihi is comprised of multiple eruptions over a single eruptive period as within-field contacts are not mappable to the same extent separate fields representing separate eruptive periods are (Sinton et al., 2002). In the north, the Aldo-Kihi overlies the older, partially delineated Rehu Marka flow field which extends to the northwest.

Aldo-Kihi is an example of a single eruptive episode with high geochemical heterogeneity. This flow field exhibits along-axis variation in MgO wt% within a range of 7.7-8.4%. Only wt% greater than 8% were found south of 17°30'S (Sinton et al., 2002). Collapse troughs, lava tubes, and lava channels between 17°26'S and 17°38'S are thought to represent the eruptive center, implying along-axis variation is due to dikes tapping into a magma chamber that was also variable along axis (Bergmanis, 1999). Even accounting for this variability, Aldo-Kihi

is geochemically distinct from Rehu Marka, which exhibits higher Fe and Ti values (Sinton et al., 2002).

18°S

The region between 18°34'S and 18°42'S contains at least three mapped flow fields. From oldest to youngest, they were identified as Next Oldest, Animal Farm, and Buddha (Sinton et al., 2002). The Animal Farm flow field between 18°34'S and 18°40'S (Figure 6) is dominated by lobate and pillow lavas in the north and sheet flows in the rest of the unit. The flow field is lightly sedimented (Sinton et al., 2002) corresponding with a paleointensity age estimate of less than 100 years (Bowles et al., 2005; Carlut and Kent, 2000). Around 18°37'S, there are channels of smooth lava with textured banks between the axial summit and a collapsed lava pond, indicating high discharge rates where the outer edges of the lava flow cool and are jumbled by the still hot, liquid inner flow(Auzende et al., 1996). Southern hydrothermal activity is similar to the first type seen at 17°25'S with warm water discharge and motile animals suggesting recent emplacement (Auzende et al., 1996).

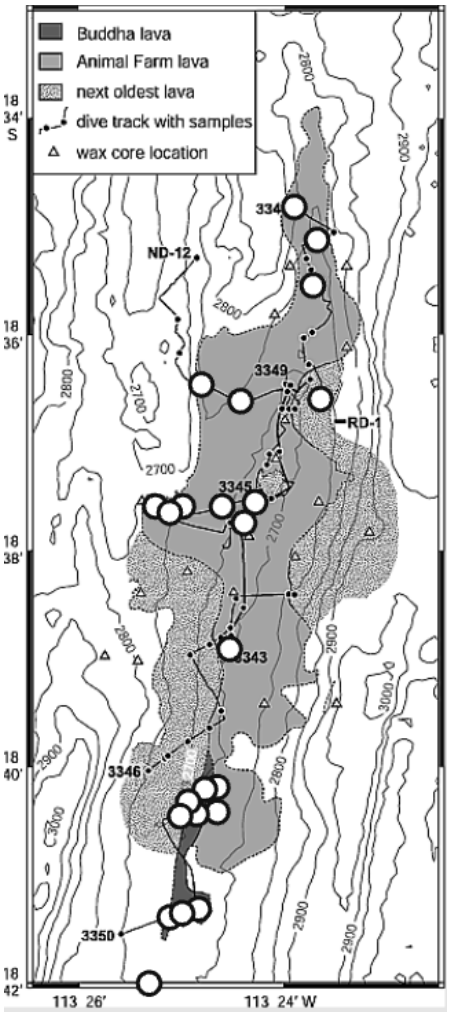

Figure 6: Dives at 18°S on the SEPR. White circles are sampling sites selected for this study. Samples were selected to be in one of the three fields: Animal Farm, Buddha, and Next Oldest (modified from Sinton et al., 2002).

The Buddha flow field between 18°40'S and 18°42'S is thought the be the youngest in the area (Sinton et al., 2002). It exhibits little sedimentation on its lobate lavas and features at

least one active hydrothermal site. Both flow fields are primarily lobate flows so the difference in sedimentation is likely due to different emplacement ages rather than influenced by morphology (Auzende et al., 1996).

There is a contrast in sediment cover between the Buddha and Next Oldest flow fields, with Next Oldest exhibiting a higher degree of sedimentation. Animal Farm and Next Oldest have a very low sediment cover contrast but are geochemically distinct possibly indicating recharge from the mantle occurring during a short interval between emplacement of the two flow fields. Next Oldest has a distinctly higher MgO content than the two other flow fields, possibly indicating a mantle recharge event, while Animal Farm and Buddha are chemically indistinguishable with MgO contents of 7.2-7.4 wt% (Sinton et al., 2002).

Methodology

Samples were collected in 1994, 1996, and 1999 via submersible and are well located with respect to observed or inferred flow field boundaries reported in Sinton et al. (2002). Typically, one sample, or basalt rock with (ideally) glassy flow top, was selected from each site location in the two regions described above (Figure 5, Figure 6). Paleomagnetic specimens are sub-samples measured in the lab. In this case, the specimens are the glass chips from the chilled margin of the basalt samples. In the 17°S region, specimens from inside and outside Aldo-Kihi and Rehu Marka were selected to compare variation within and between different flow fields (Figure 4). In the 18°S region, specimens from inside and outside Buddha, Animal Farm, and Next Oldest were selected. Glass specimens (as opposed to crystalline rock) are used for this project as they cool quickly, preserving paleointensity near eruption timings and resulting in small magnetic particles, which demonstrate ideal behavior in paleointensity experiments (Bowles et al., 2006).

Sample Selection and Preparation

One hundred thirty-eight SBG specimens with magnetic moments greater than 10^{-10} Am² were selected using a 2G Enterprises 755SRMS Superconducting Rock Magnetometer to have a reasonable signal:noise ratio. The constraint on magnetic moment was due to the sensitivity of the magnetometer. For sites with no suitable specimens, moments up to an order of magnitude weaker were selected. This process resulted in 2-5 glass specimens per sample. Labeled glass vials and selected specimens were soaked in a 10% HCl dilution to remove superficial Fe staining or contamination. Each specimen was secured in a 1-cm diameter glass vial with glass microfiber filters and potassium silicate to prevent movement during measuring (Figure 7).

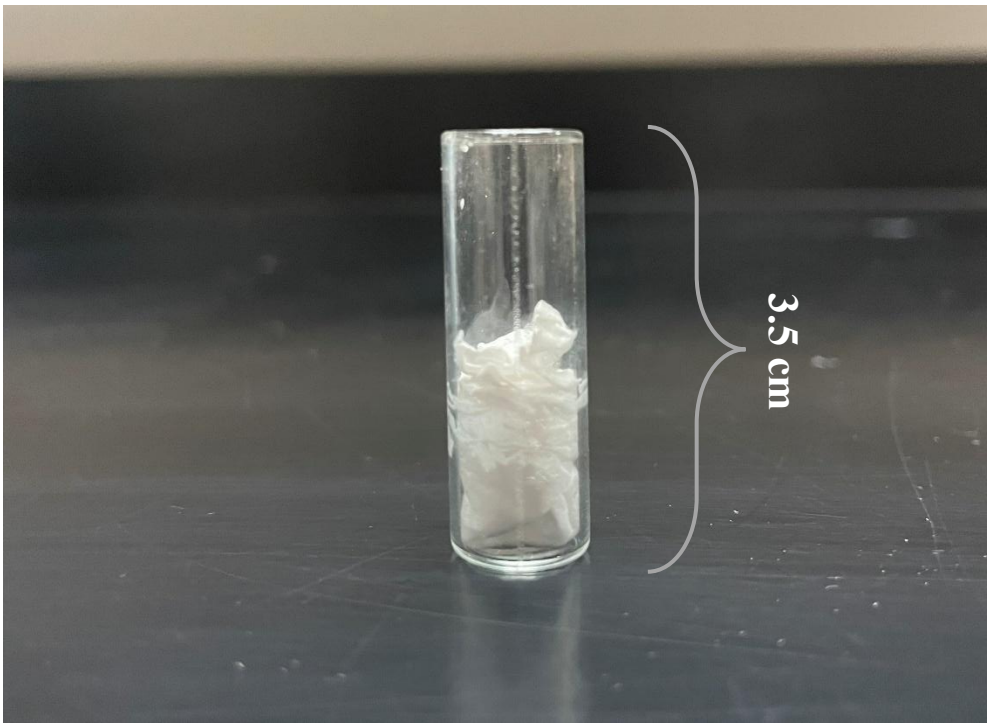

Figure 7: Glass vial containing secured SBG specimen.

Paleointensity Methods

Paleointensity experiments followed the IZZI method (Yu et al., 2004),where the order of the in-field (I) and zero-field (Z) steps alternates with each temperature step. A 40 μT field was used for the in-field steps, and the zero-field was measured to be less than -0.0709 μT before each zero-field step. pTRM checks were conducted every other temperature step with the ZI steps. Samples were heated in an ASC Thermal Demagnetizer with a TRM coil for in-field steps. All heating and measurements took place inside a magnetically shielded room at the University of Wisconsin – Milwaukee. Data were analyzed using PmagPy software (Tauxe et al., 2016).

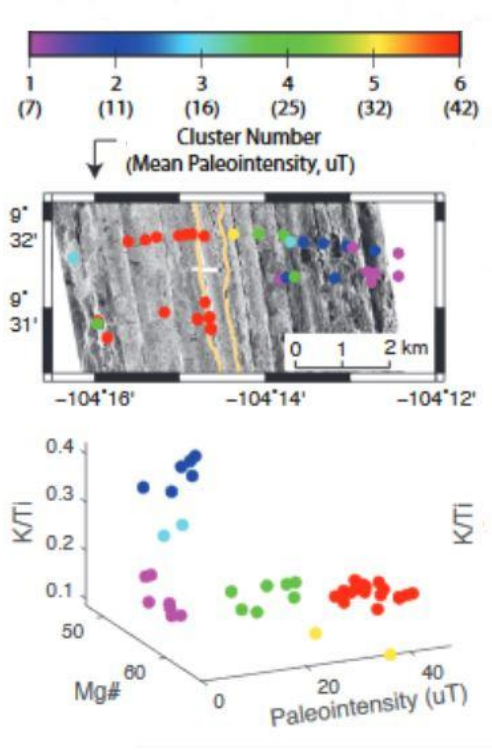

Figure 8: Cluster analysis applied to paleomagnetic and geochemical data from 9°30'N EPR. Color indicates a cluster of mean paleointensity. Tan lines are troughs at the crest of the ridge. Samples have a paleointensity standard error of <2.5 μT. (modified from Bowles, unpublished).

Cluster Analysis

A cluster analysis is used to jointly evaluate the paleointensity and geochemistry data for eruptive clusters (Figure 8). Cluster analyses are algorithms for grouping data such that data within a single group or cluster are more similar to each other than data in a separate group. There are two main groups of clustering algorithms: hard and soft. Data in hard algorithms can only belong to one cluster. Data in soft algorithms can belong to more than one cluster. The model of interest is a soft Gaussian mixture model (GMM), which assumes the data clusters have a normal distribution and assigns the likelihood of a data point belonging to different clusters (Figueiredo and Jain, 2002). In this model, clusters can be different sizes and have different covariance structures, although we have applied a constraint that forces clusters to share the

same internal covariance structure. We also assume a diagonal covariance structure, which means the variables (paleointensity and geochemistry) are not correlated.

The method also allows for an unknown number of clusters prior to execution. The optimal number of clusters, implied to be indicative of the true underlying structure of the data, can be ambiguous and various methods have been developed for determination. The criterion used in this instance is the Bayesian information criterion (BIC) which measures how well the model fits the data while penalizing complexity (number of clusters) to prevent overfitting (e.g., Sadeghi, 2025). The GMM cluster analysis is performed for a range of cluster numbers (in this case, up to nine clusters), and the model with the minimum BIC represents the optimal number of clusters. The ideal outcome would be for the GMM-determined clusters to match the previously identified flow fields.

The variables included in the cluster analysis are paleointensity (representing time), magnesium number (Mg#) reflecting how evolved a magma is (degree of fractionation), and K/Ti which is related to the mantle source. Figure 8 shows this approach applied to a dataset on the 9°N segment of the EPR (Bowles, pers. comm.). Flow fields with a similar geochemistry, such as Cluster 1 and Cluster 4, are distinguished on the basis of different paleointensities. Likewise, flow fields with similar paleointensities such as Clusters 1, 2, and 3, can be distinguished from each other by different geochemical compositions, in this case differing K/Ti. In this example, flow field boundaries are unknown, and the present work will test the approach in a region with known flow field boundaries.

Results

Paleointensity Results

Specimens (Appendix A) used represented 13 samples from 17°S and 23 samples from 18°S. At 17°S, there were 4 samples from Aldo-Kihi, 3 from Rehu Marka, 4 from Neither A, and 2 from Neither B. At 18°S, there were 13 samples from Animal Farm, 5 from Buddha, and 5 from Next Oldest. Interpreted paleointensities ranged from 28.8 to 44.6 μT at 17°S and 4.80 to 55.6 μT at 18°S.

Specimens were split between those that displayed ideal Thellier behavior with linear or approximately linear Arai plots (Figure 9) and those displaying distinctly non-linear behavior (Figure 10). Passing pTRM checks are also an indicator of high-quality data as they suggest an absence of mineral alteration. Single-direction Zijderveld plots decaying to the origin support a single component of magnetization in the NRM. Deviation from these trends, such as curved Arai or Zijderveld plots, could indicate mineral alteration during heating steps or the presence of multi- domain particles which could result in less reliable paleointensities

Slope Selection

Sections of each Arai plot were picked to identify the most stable magnetization as it likely represents the original magnetization of the specimen. These slope sections were handpicked to exclude any low-temperature viscous overprint while still including as many temperature steps for each specimen as possible (Figure 9, 10). In cases of discrepant slopes in a specimen, the high-temperature portion was selected. Slopes were also selected to correspond to single component segments on the Zijderveld plot. Final selection of specimens for interpretation

was done by applying quality control selection criteria (Table 1) and determining if the standard deviation of the sample average improved.

Several specimens from Aldo-Kihi with weak moments ($<4 \times 10^{-9}$ Am^2) displayed anomalous behavior during the in-field 100°C temperature step. This behavior is not physically realistic and may arise from not accurately accounting for the magnetic moment of the sample holder. For these specimens, the 100°C step was discarded.

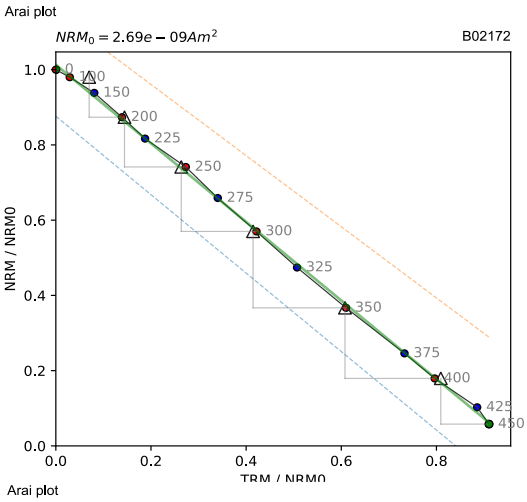

Zijderveld B02172

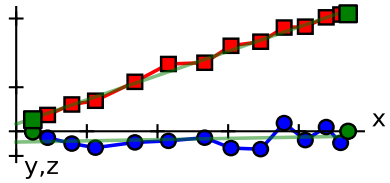

SCAT	DANG	MAD_{free}	DRATS
Pass	3.7	4.1	4.4

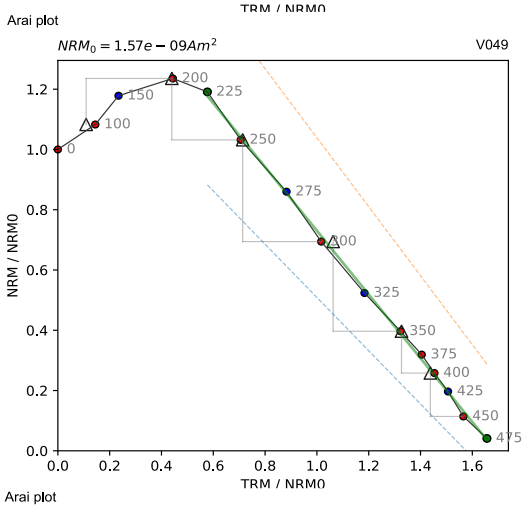

Zijderveld V049

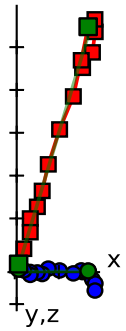

SCAT	Pass
DANG	0.2
MAD_{free}	1.8
DRATS	0.2

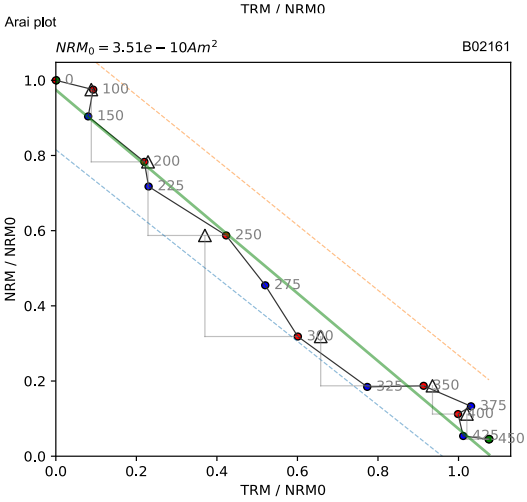

Zijderveld B02161

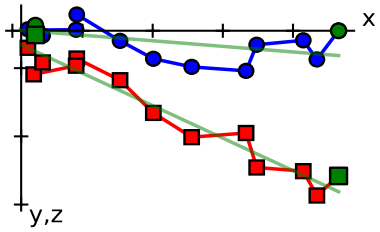

SCAT	DANG	MAD_{free}	DRATS
Pass	4.7	8.5	4.9

Figure 9: Acceptable slope sections displaying possible behaviors: ***B02172)*** *Ideal plots displaying linear behavior. Zijderveld plot decays to the origin.* ***V049)*** *Isolated higher temperature slope displays similar behavior to B02172.* ***B02161)*** *Arai plot with increased scatter, but still within established tolerance (passes SCAT criteria). Approximated Zijderveld slopes decay to the origin.*

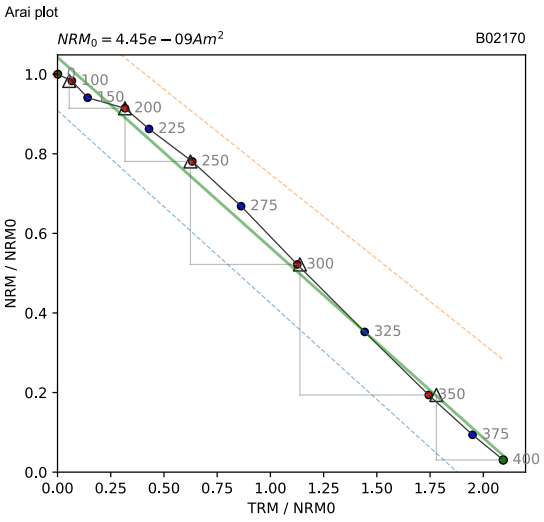

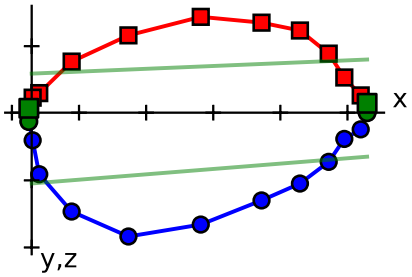

SCAT	DANG	MAD_{free}	DRATS
Pass	25.4	20.8	1.3

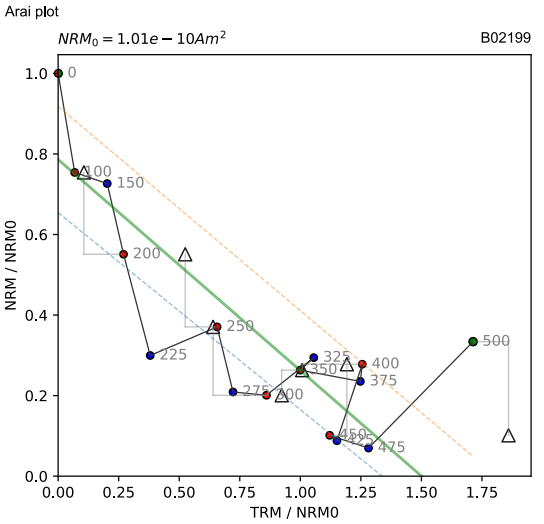

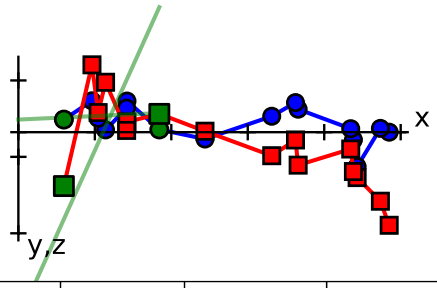

SCAT	DANG	MAD_{free}	DRATS
Fail	31.5	22.2	59.7

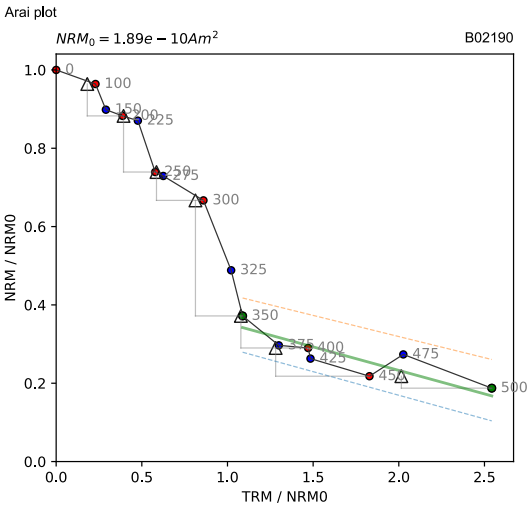

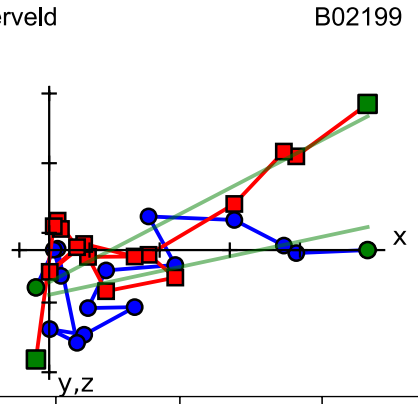

SCAT	DANG	MAD_{free}	DRATS
Pass	56.2	37.3	3.7

Figure 10: Problematic slope sections displaying possible behaviors: ***B02170)*** *Non-linear Zijderveld plot.* ***B02199)*** *High-scatter poor approximation of linear behavior.* ***B02190)*** *Low number of data points used for slope and poor approximation of linear behavior.*

Selection Criteria

Cumulative distribution function (CDF) plots were created to understand the overall distribution of the different selection criteria and as an aid in setting threshold values (Figure 11). Due to limited specimens available for each site, selection criteria were chosen to maximize the number of specimens chosen for analysis while still accurately representing the data (Table 1). A range of common statistics and thresholds (Paterson et al., 2014) were tested, then refined by trial and error to determine which statistics seemed to have a greater effect on site specific standard deviation.

Paterson et al. (2012) modeled the behavior of ideal single-domain grains and the distribution of their selection statistics. The 95th percentile of the selection statistic distributions were used to modify selection criteria found in previous studies (e.g. Bowles et al., 2006). These modified criteria sets slightly increase the risk of accepting inaccurate results (paleointensity estimate greater than 10% of expected value), but allow for a relatively large increase in acceptance of accurate results (Paterson, 2014). Personal discretion resulted in final usage of some statistics not included in the modified sets but which are related and measure the same behavior (such as DRATS instead of DRAT, see below). The 17°S and 18°S regions were evaluated separately.

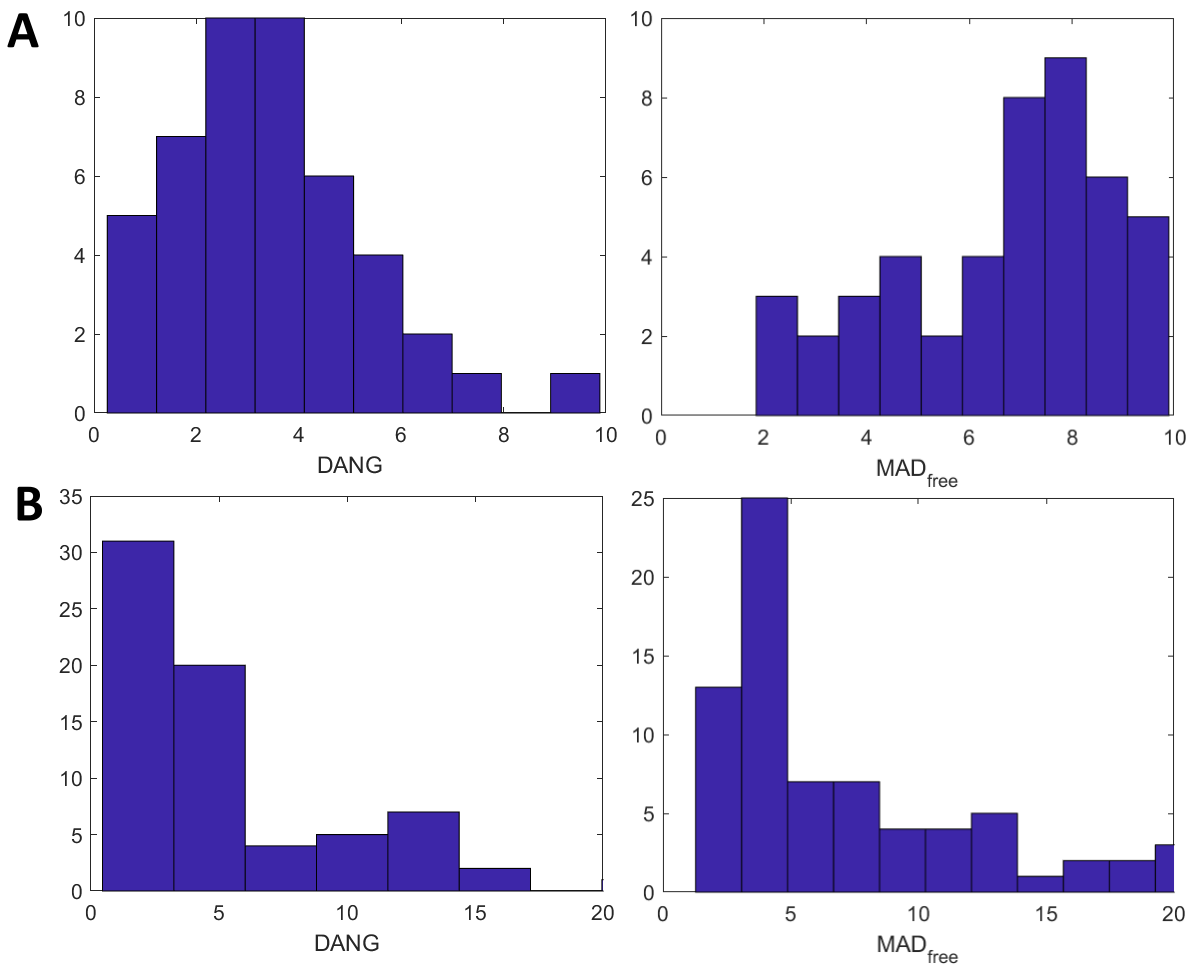

Figure 11: Histograms of DANG and Mad_{free} for A) 17°S region and B) 18°S region.

Table 1: Selection criteria for 17°S and 18°S. FRAC and f are related to the fraction of NRM used for the slope selection (Coe et al., 1978 and Shaar and Tauxe, 2013). FRAC and f display minimum values while the rest are maximum values. Every specimen passed f, FRAC, and β. DANG and MADfree appeared to have the greatest effect on sample standard deviations.

Statistic	17°S	18°S
f	0.35	0.35
FRAC	0.35	0.35
SCAT	PASS	PASS
DANG	9	11
DRATS	9	11
DRAT	10	11
MAD_{free}	10.5	10.2
β	0.155	0.155

There are two selection statistics related to scatter in the Arai plot: β and SCAT. β is a measure of relative scatter in the data around the best-fit slope and is the ratio of the standard error of the slope to the absolute value of the slope (Coe et al., 1978). SCAT, as proposed by Shaar and Tauxe (2013), also tests scatter on the Arai plot, including pTRM checks. It uses error from the best-fit Arai slope to determine whether selected data are too scattered. A specimen can only pass or fail, resulting in TRUE if it passes or FALSE if it fails. The exact parameters of SCAT are determined by β, so β was increased from the value of 0.100 used in the majority of criteria sets (Paterson et al., 2014) to 0.155 so as to include data that originally barely failed SCAT.

Other statistics related to pTRM checks on the Arai plot are the difference ratio (DRAT) and the difference ratio sum (DRATS). DRAT is the maximum absolute difference produced by a single pTRM check, normalized by the length of the best-fit line (Selkin et al., 2000). It shows the maximum difference between the magnetization during the original temperature step and the magnetization of the pTRM check at the same temperature. A smaller difference means the magnetic acquisition capacity of the specimen has not changed. DRAT is only the maximum value so could be affected by a single large outlier or by a low signal:noise ratio common in the more weakly-magnetic specimens. As a result, we also looked at DRATS. DRATS is the cumulative, signed difference of pTRM checks normalized by the pTRM gained during the maximum temperature step on the best-fit slope (Tauxe and Staudigel, 2004). Because it is cumulative, random difference due to noise should be cancelled out while outliers should be minimized.

The NRM directions are assessed with two statistics: the free floating maximum angular deviation ($MAD_{free)}$ and the deviation angle (DANG). MAD_{free} is a measure of scatter between each magnetic component and the best-fit line (Kirschvink, 1980). It is free-floating when the best fit direction is determined solely by the components and not anchored to the origin of the Zijderveld plot. Lower MAD_{free} values indicate a lower level of scatter and more precise data. DANG is the angle between the best-fit line and the line connecting the center of mass and the origin (Tanaka and Kobayashi, 2003; Tauxe and Staudigel, 2004). Specimens with low DANG values decay to the origin on the Zijderveld plot, indicating that a stable NRM direction has been isolated. DANG was not present in the modified criteria; however, it (along with MAD_{free}) appeared to have the greatest effect on sample standard deviation.

Sample Acceptance

Around 17°S, paleointensity site means range from 28.1 to 42.7 μT. Eleven out of 13 sites had specimens pass the acceptance criteria and were combined with 7 sites from previous studies (Carlut and Kent, 2000; Bowles et al., 2005; Bergmanis et al., 2007) including within Aldo-Kihi and Rehu-Marka and outside of both. The 7 additional sites expanded the upper limit of the paleointensity range to 45.1 μT (Table 2). Site means around 18°S range from 27.0 to 48.9 μT. Twenty out of 23 sites passed the acceptance criteria. Out of those 20 sites, 3 were discarded as only a single specimen passed**.** Two of those discarded sites are within Animal Farm (AL3345-4 and ND12-5) and have paleointensities similar to the majority of Animal Farm paleointensities. The other site is within Next Oldest (AL3346-10) and is similar to the higher of the two Next Oldest specimens (AL3346-1). Three more sites were discarded as zero specimens passed.

Additionally, AL3346-3 was also discarded due to an anomalously high standard deviation (7.9 μT). The 13 selected samples were combined with 6 samples from previous studies outside of Aldo Kihi and Rehu Marka resulting in 19 samples and expanding the upper limit of the range to 58.9 μT (Table 3) (Carlut and Kent, 2000; Bergmanis et al., 2007; Bowles et al., 2005).

Table 2: Paleointensity and geochemical data for accepted specimens in sites around 17°S.

Site	Lon	Lat	Pint (μT)	St Dev	n	Mg#	K/Ti	Flow Field
ND20-5	-113.208	-17.442	30.8	0.9	5	55.8	0.116	Aldo-Kihi
AL3357-3	-113.224	-17.4653	31.9	0.4	5	57.9	0.119	Aldo-Kihi
AL3364-2	-113.221	-17.4507	28.1	3.1	3	58.1	0.0781	Aldo-Kihi
ND3-5[1]	-113.206	-17.4287	30	0.8	8	57.8	0.117	Aldo-Kihi
AL3360-8[1]	-113.219	-17.4855	32.2	0.7	5	59.1	0.113	Aldo-Kihi
AL3363-7[1]	-113.236	-17.5438	28.6	2.2	3	59.8	0.117	Aldo-Kihi
AL3357-1	-113.228	-17.4647	37.8	2.2	2	53.1	0.128	Neither (A)
ND4-02	-113.197	-17.3918	42.7	1.5	5	56.9	0.137	Neither (A)
ND4-03	-113.197	-17.3975	39.2	1.9	3	58.1	0.146	Neither (A)
ND5-09	-113.195	-17.3885	38.6	1.8	5	57.6	0.120	Neither (A)
AL3357-2	-113.227	-17.4657	30	1.0	5	56.8	0.126	Neither (B)
AL3364-1	-113.226	-17.4506	32.8	1.1	5	56.6	0.126	Neither (B)
ND6-1[1]	-113.198	-17.4045	33.9	1.0	6	58.5	0.145	NW of Aldo-Kihi
ND18-1[1]	-113.202	-17.415	38	0.7	8	52.7	0.184	Rehu Marka
ND3-02	-113.214	-17.4208	33.6	3.2	5	52.1	0.178	Rehu-Marka
ND3-03	-113.209	-17.426	35.3	3.5	2	52.4	0.170	Rehu-Marka
AL3359-2[1]	-113.238	-17.56	32.5	0.5	12	58.4	0.166	SE of Aldo-Kihi
AL3361-4[1]	-113.233	-17.5183	45.1	1.7	12	62.7	0.166	W of Aldo-Kihi

[1]Data from Bowles et al., 2005.

Table 3: Paleointensity and geochemical data for accepted specimens in sites around 18°S.

Site	Lon	Lat	Pint (μT)	St Dev	n	Mg#	K/Ti	Flow Field
AL3344-1	-113.398	-18.5802	27	0.5	2	41.0	0.0485	Animal Farm
AL3344-4	-113.395	-18.5855	48.9	0.6	3	40.5	0.0424	Animal Farm
AL3344-7	-113.396	-18.5922	30.2	2.3	3	40.5	0.0536	Animal Farm
AL3344-6[2]	-113.396	-18.590	35.2	0.5	8	54.8	0.0807	Animal Farm
AL3344-9[2]	-113.396	-18.599	35.1	1.6	5	54.7	0.0908	Animal Farm
AL3344-10[2]	-113.397	-18.600	35.8	0.2	6	54.9	0.0908	Animal Farm
AL3345-7	-113.421	-18.6265	47.6	1.8	2	40.7	0.0588	Animal Farm
AL3346-16	-113.399	-18.7268	38	2.2	2	41.6	0.0432	Animal Farm
AL3349-2[2]	-113.4165	-18.607	32.5	1.0	6	55.8	0.0832	Animal Farm
AL3350-8	-113.411	-18.672	35.8	0.8	4	41.3	0.0488	Animal Farm
ND12-6	-113.407	-18.6102	30.5	1.8	4	37.6	0.0303	Animal Farm
AL3350-10	-113.413	-18.668	33.8	0.4	4	40.9	0.0539	Buddha
AL3350-2	-113.419	-18.69	39	3.7	2	41.0	0.0552	Buddha
AL3350-3	-113.417	-18.689	31.1	1.0	3	41.1	0.0482	Buddha
AL3350-6	-113.414	-18.673	35	1.0	3	41.0	0.0542	Buddha
AL3344-12	-113.394	-18.6097	33	1.7	5	44.5	0.0470	Next Oldest
AL3346-1	-113.422	-18.6997	37.8	2.0	4	45.5	0.0423	Next Oldest
AL3352-3[1]	-113.35	-18.179	38.6	1.4	5	59.4	0.0612	Moai
AL3353-7[1]	-113.38	-18.348	35.8	1.2	6	60.5	0.0493	Lava Shield
AL3356-1[1]	-113.34	-18.216	55	2.9	5	57.6	0.0688	SE of Moai
AL3354-10[1]	-113.37	-18.299	58.9	3.1	3	52.9	0.0464	older flow field? Inside graben
AL3348-5[1]	-113.41	-18.531	45.7	1.1	7	54.7	0.0586	N South Hump

Site	Lon	Lat	Pint (μT)	St Dev	n	Mg#	K/Ti	Flow Field
AL3347-5[1]	-113.42	-18.572	37.3	1.0	6	45.4	0.0548	S South Hump
AL3345-4	-113.41	-18.626	29.8	1.0	1	54.8	0.0807	Animal Farm
AL3346-10	-113.41	-18.72	38.3	1.0	1	60.5	0.0830	Next Oldest
ND12-5	-113.41	-18.608	28.6	1.0	1	53.8	0.0948	Animal Farm

[1]Data from Bowles et al., 2005. [2]Carlut and Kent, 2000.

Emplacement Dates

To determine emplacement dates, two different field models were evaluated: the CALS10k.2 and HFM.OL1.A1 models. Both models are based predominantly on sediment records but are calibrated to absolute paleointensity using volcanic and archaeomagnetic data. For the most recent ~400 years, the CALS10k.2 is forced to agree with the *gufm1* model (Jackson et al., 2000) which is based solely on historical observations. The HFM.OL1.A1 model does not share this constraint – it is based only on the paleomagnetic data.

All included samples are thought to have formed relatively recently, where the monotonically decreasing field can provide absolute age estimates. Sample level age estimates are shown in Appendix B. Global field models (Constable et al., 2016) evaluated at 17°S indicate possible emplacement dates from 1800 to present day (Figure 12). Aldo-Kihi is indistinguishable from the present day, while Rehu Marka and the flow field to the north of Aldo-Kihi (referred to as Neither A) appear to be older. An unnamed flow field to the west of Aldo Kihi is referred to here as Neither B and seems to be of a similar age to Aldo-Kihi. These results agree with dive observations (Table 4) that determined Aldo-Kihi to be the youngest flow field (Sinton et al., 2002)

Global field models (Constable et al., 2016) evaluated at 19°S indicate possible emplacement dates between 1850-1950 for the 18°S region (Figure 13). Based on paleointensity, Buddha is determined to be the youngest flow field, followed by Next Oldest, then Animal Farm. Based on dive observations, however, Buddha is likely the youngest, but Next Oldest is the oldest (Table 4). Also based on dive observations, the estimated recurrence interval between the three flow fields is a few years to a few decades, and this is supported by the paleointensity data.

The sediment cover contrast between Buddha and Animal Farm is greater than between Animal Farm and Next Oldest, implying a greater age difference, but all three flow fields were emplaced within a short time period (Sinton et al., 2002). The overlapping emplacement dates could reflect the short recurrence interals thought to exist between these flows.

Table 4: Dive observations (Sinton et al., 2002) differentiating each flow field in the 17°S and 18°S region. Flow fields in stratigraphic order with youngest at the top, except for Neither B as dive observations do not identify relative age relationships. Age estimates determined by the method referenced in Figure 12. Final estimates are averaged from HFM and CALS10k field models (Figure 12, Figure 13).

Flow	Dive Observations	Paleointensity Age Estimate
	17°S	
Aldo-Kihi	very little sediment cover, flow morphology contacts, some contacts identified based on geochemistry, evidence for multiple flows during one episode	10 ± 29 years old
Rehu Marka	distinctive Fe and Ti rich composition	125 ± 53 years old
Neither A	similar composition to younger Aldo-Kihi lavas but more sedimented	211 ± 40 years old
Neither B	not defined outside of flow identification	24 ± 24 years old
	18°S	
Buddha	compositionally identical to Animal Farm, lower sedimentation than Animal Farm	120 ± 40 years old
Animal Farm	lightly sedimented, previous paleointensity ages indicate flow is around 100 years old	135 ± 26 years old
Next Oldest	higher MgO, very low sediment contrast with Animal Farm, emplaced underneath Animal Farm	106 ± 33 years old

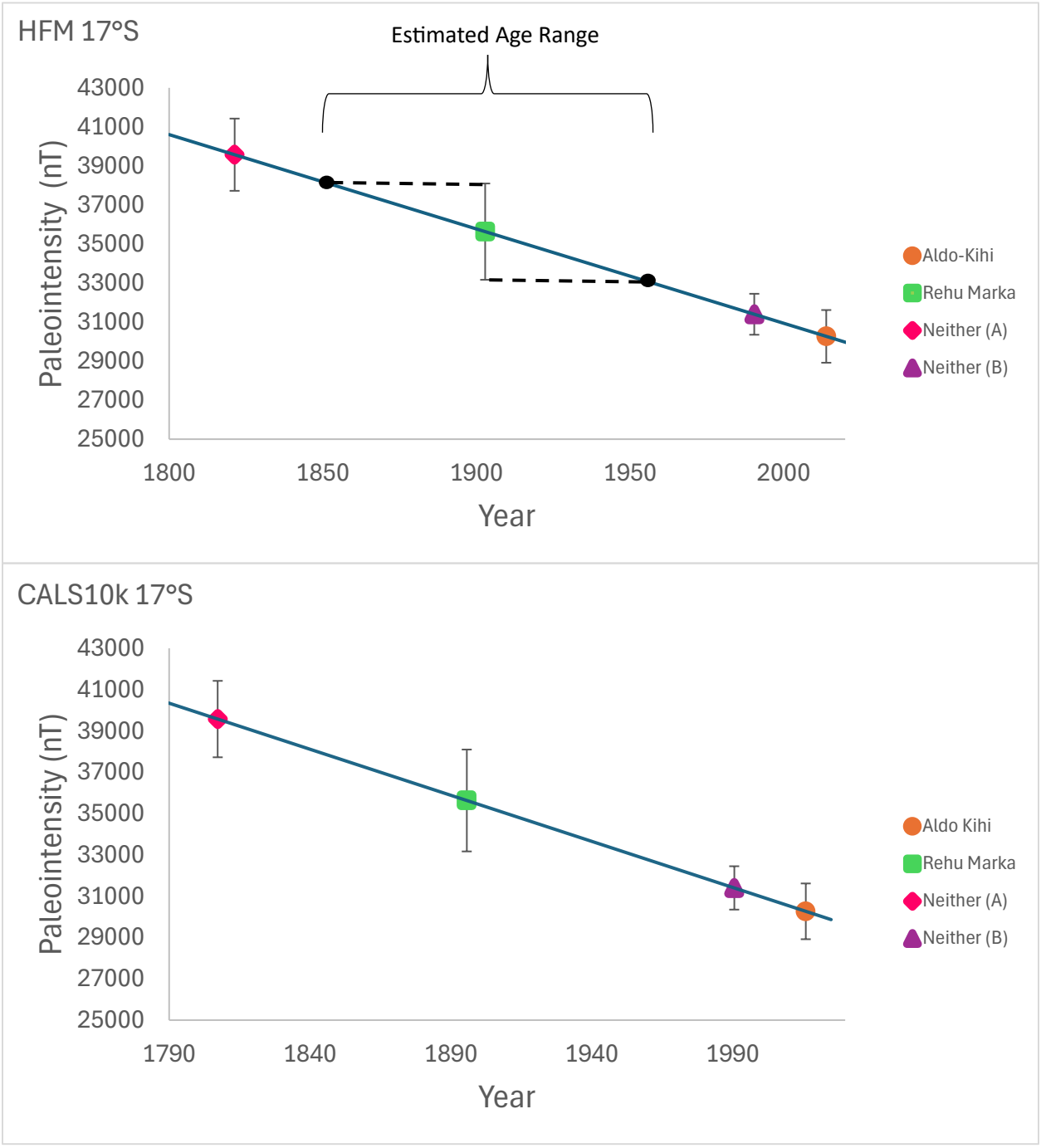

Figure 12: Flow field mean paleointensities and corresponding emplacement ages determined from CALS10k and HFM field models (Figure 2) evaluated at 17°S (Constable et. al., 2016). Aldo-Kihi and Rehu Marka means include previously collected data (Bowles et al., 2005). Error bars indicative of scatter in site paleointensities and not necessarily representative of overall uncertainty. HFM 17°S shows determination of upper and lower age estimates (black) for a flow field. Estimates made for all flow fields for both models.

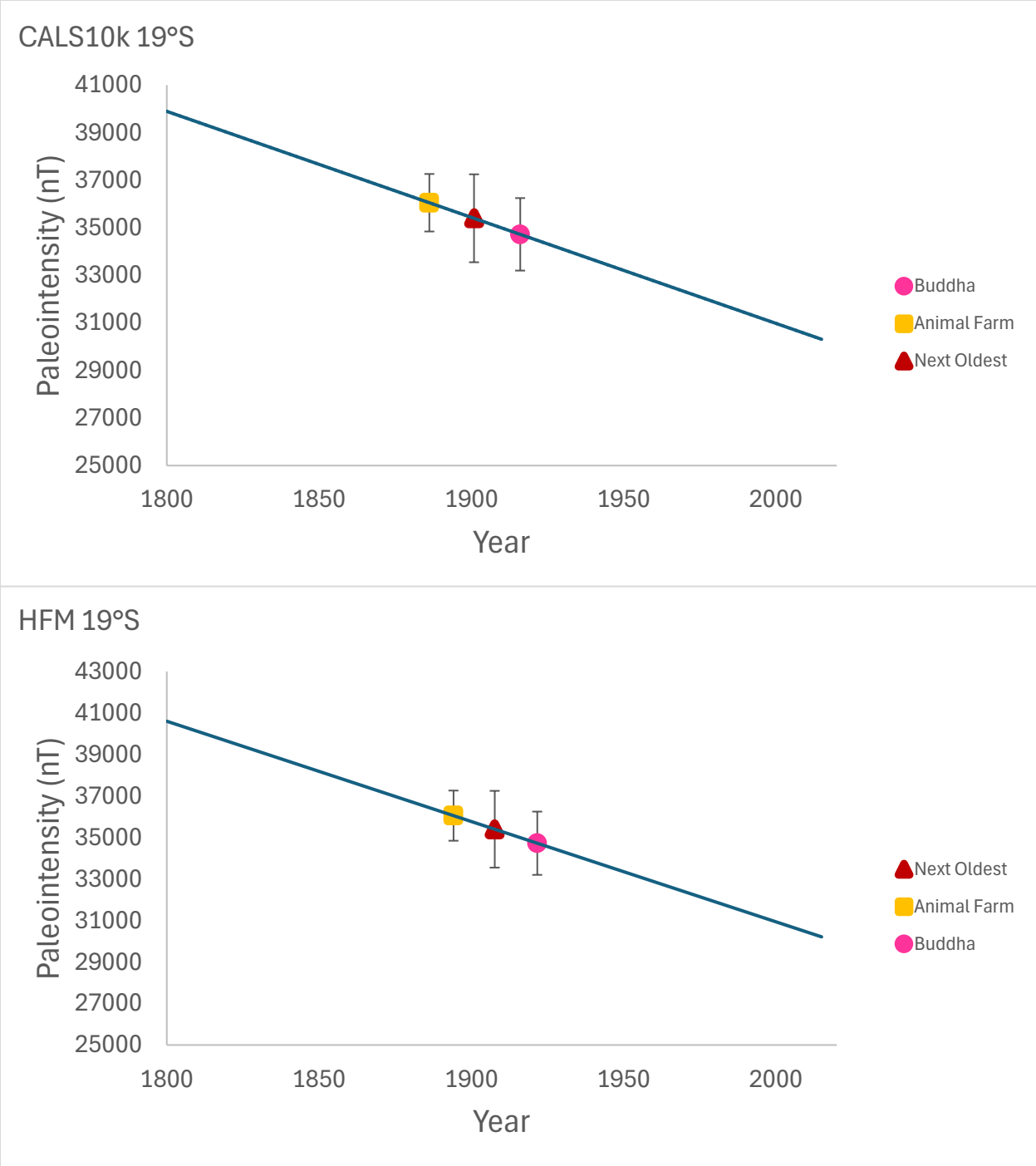

Figure 13: Flow field mean paleointensities and corresponding emplacement ages determined from CALS10k and HFM field models (Figure 2) evaluated at 19°S (Constable et. al., 2016). Animal Farm means include previously collected data (Bowles et al., 2005; Carlut and Kent, 2000). Error bars indicative of scatter in site paleointensities and not necessarily representative of overall uncertainty. Age estimates determined by the method referenced in Figure 12.

Cluster Analysis

Within the region at 17°S (Figure 14), the cluster analysis is optimized with four clusters, indicating the data contain samples from four different flow fields (Figure 15). The cluster corresponding to the Aldo-Kihi flow (blue) includes samples originally categorized as Neither B (AL3357-2 and AL3364-1) and a 17°S outflow sample to the southeast (AL3359-2). ND18-1 is another 17°S outflow sample near the Aldo-Kihi flow boundary but it is not grouped with the rest and is instead in a cluster by itself (brown), indicating it may belong to a completely different flow from other samples. Rehu Marka samples (green) cluster together as expected due to its higher paleointensity and distinctive composition. Samples categorized as Neither A (orange) appear to belong to a separate flow, except for one which is grouped with Rehu Marka samples but at a probability less than 98%.

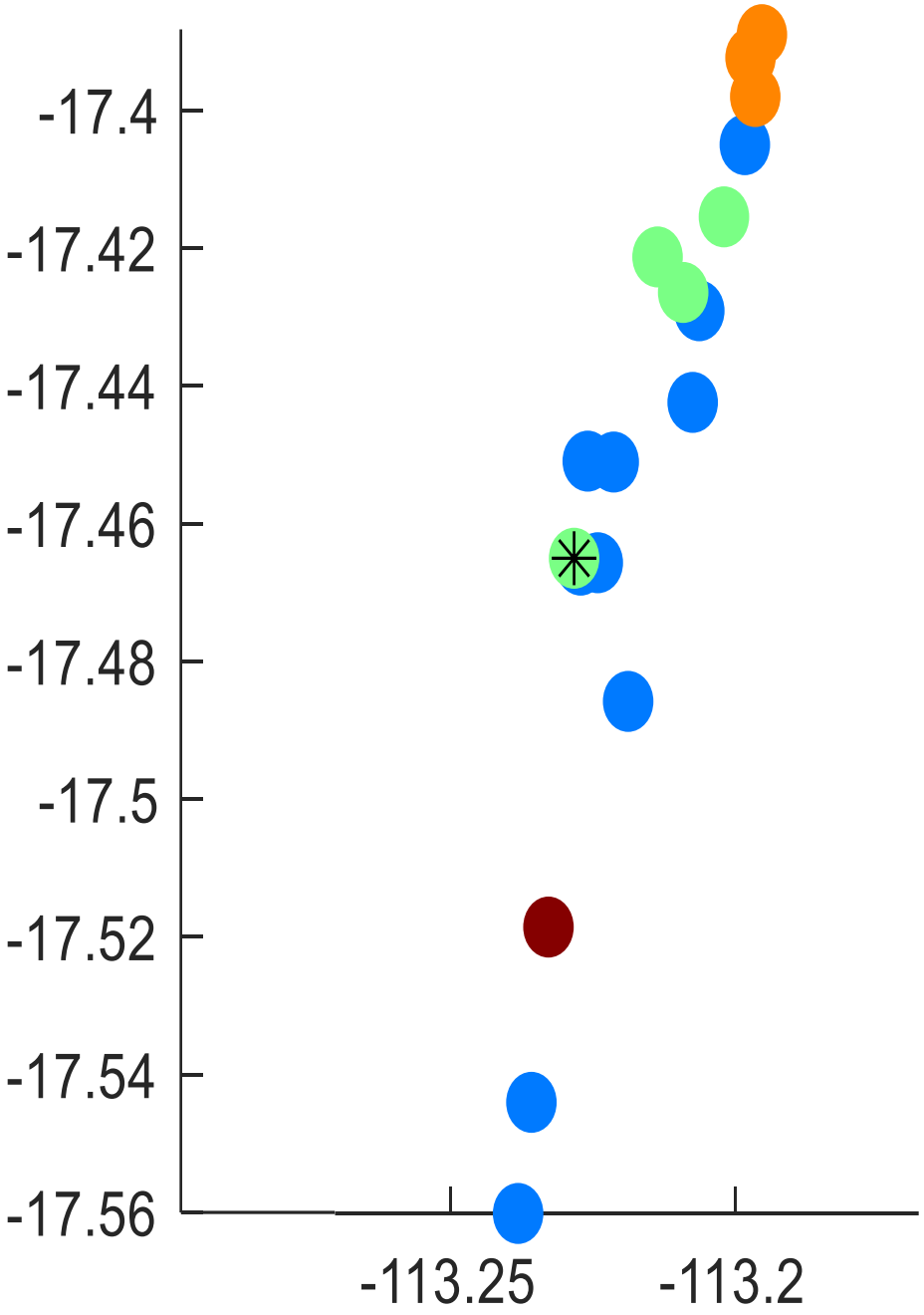

Figure 14: Location of sample sites in the 17°S region, colored to indicate cluster membership. Asterisked sample indicates cluster membership to be less than 98%

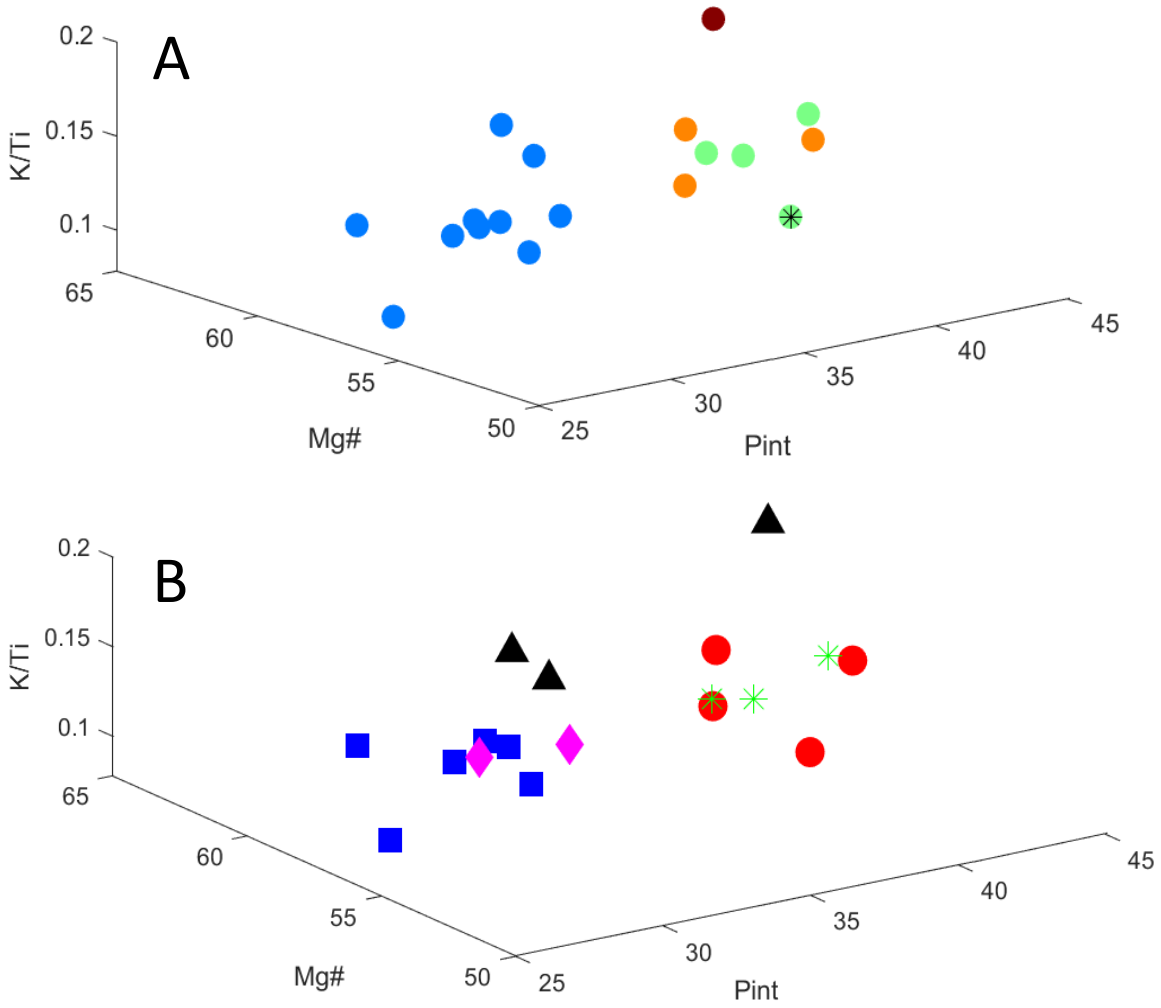

Figure 15: A) Cluster analysis based on paleointensity and geochemistry for flow field at 17°S. Asterisked sample indicates cluster membership to be less than 98% probability. B) Position of Aldo-Kihi (blue), Rehu Marka (green), Neither A (red), Neither B (pink), and 17°S outflow (black) samples in cluster analysis.

Samples from 18°S (Figure 16) are grouped into seven clusters implying seven flow fields (Figure 17). Four of these clusters represent data from flow fields further north of the 18°S region in (18°S outflow sites). One of these outflow sites is from the South Hump flow field at 18°33'S (Figure 17). 18°S outflow samples (black) cluster separately from the samples in Next Oldest, Animal Farm, and Buddha, except for AL3353-7 from the Lava Shield flow field (18°21'S) that clusters with the Next Oldest flow field (18°35'S), implying the two flow fields may originate from the same eruptive event. One of the Animal Farm samples (AL3346-16) only clusters with the rest of Animal Farm samples at a probability of less than 98%. Animal Farm (except for high-paleointensity AL3344-4 and AL3345-7) and Buddha samples cluster together. South Hump (18°33'S) is represented by samples from two different flows. The sample with a lower paleointensity and Mg# (AL3347-5) is distinct from any other sample, while the higher paleointensity sample (AL3348-5) clusters with outlier samples in Animal Farm (18°37'S) that may represent a separate flow field. The younger South Hump flow seems to have been emplaced around the same time as Animal Farm, based on paleointensity, and is only differentiated by a different geochemistry (Sinton, et al., 2002).

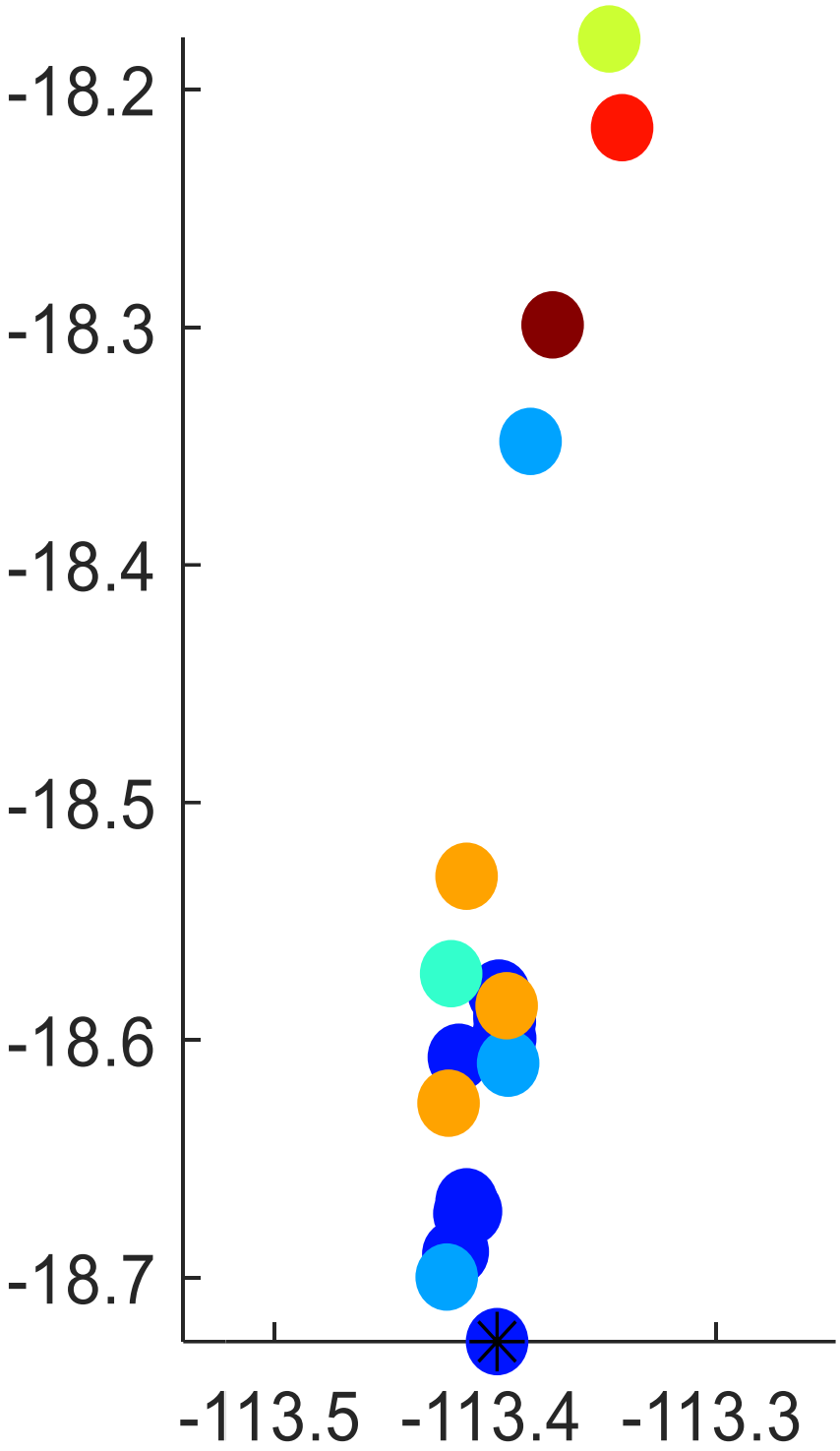

Figure 16: A) Location of sample sites in the 18°S region, colored to indicate cluster membership. Asterisked sample indicates cluster membership to be less than 98%.

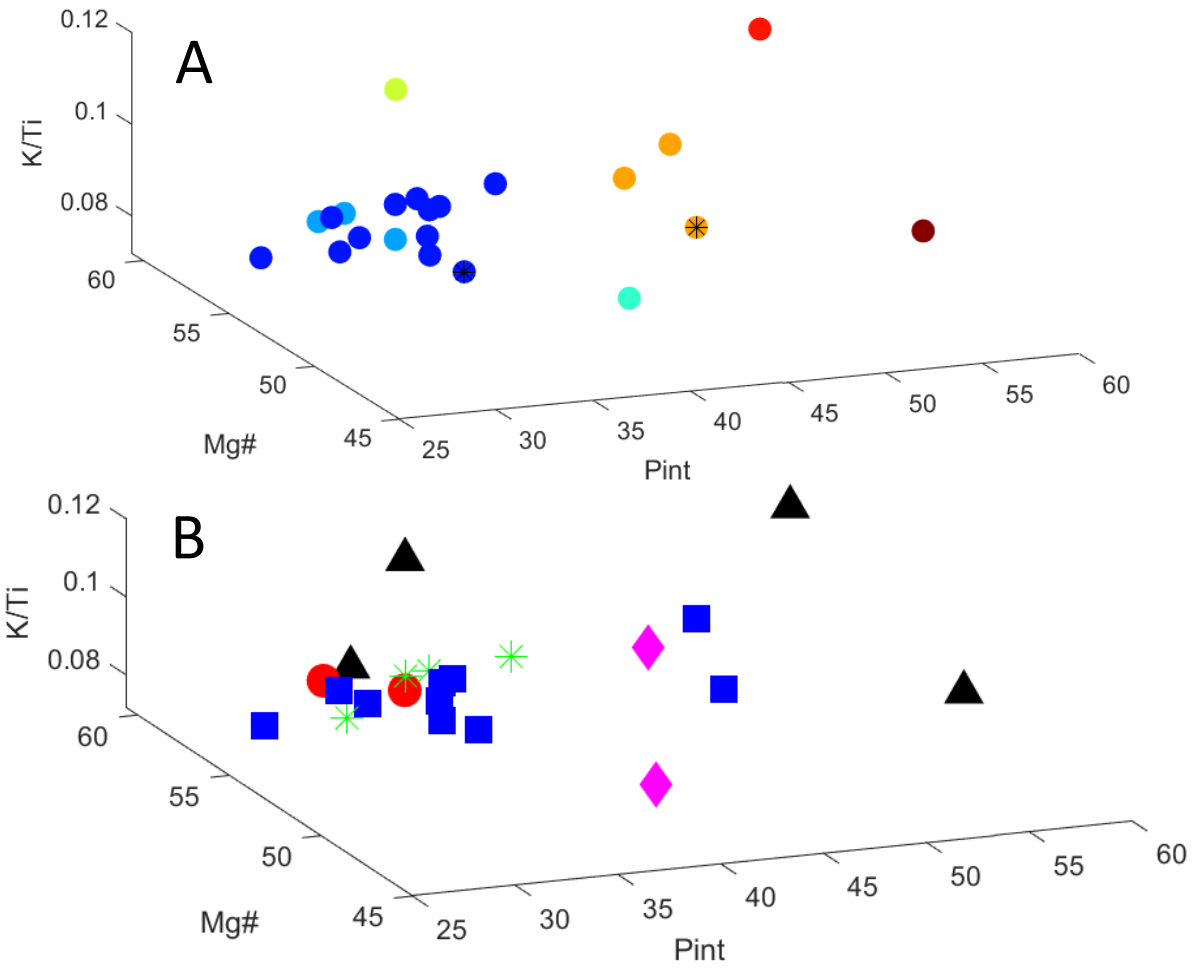

Figure 17: A) Cluster analysis based on paleointensity and geochemistry for flow fields at 18°S. Asterisked sample indicates cluster membership to be less than 98% B) Position of Animal Farm (blue), Buddha (green), Next Oldest (red), South Hump (pink), and 18° outflow (black) samples in cluster analysis. Sample ND12-6 was not included as glass geochemistry was not available.

Discussion

Paleointensity

In the 17°S region, Sinton et al. (2002) identified four flow fields based primarily on dive observations. From oldest to youngest, these are Neither A (17°23-24'S), Rehu Marka, and Aldo-Kihi. Neither B is not specifically mentioned but is identified as separate from the rest of the flow fields in this area. The relative age of this Neither B unit compared to the others is unknown, except for in relation to Aldo-Kihi where Neither B is likely older based on superposition as it is beneath Aldo-Kihi.

Based on the paleointensity data, the youngest is likely the Aldo-Kihi flow, followed closely by Neither B. These two flows share low paleointensities (Figure 14) indistinguishable from present day, indicating they likely erupted around the same time. However, the Aldo-Kihi exhibits a lower K/Ti ratio than the western flow distinguishing the two. Based on superposition, Aldo-Kihi would have to be the youngest flow which agrees with an estimated emplacement age in the early 1990s (Sinton et al., 2002).

The western flow (Neither B) is also distinguished from the other category of miscellaneous samples (Neither A) in the north by their paleointensities. The northern samples have higher paleointensities indicating they could be from a separate, older flow (Figure 14). K/Ti values are also higher for northern samples as opposed to western samples. Sinton et al. (2002) classified AL3357-1 with the northern Neither A samples, but the sample is

geographically located next to Neither B samples. The northern samples have higher paleointensities than Rehu Marka (Figure 14) implying it was emplaced before Rehu Marka.

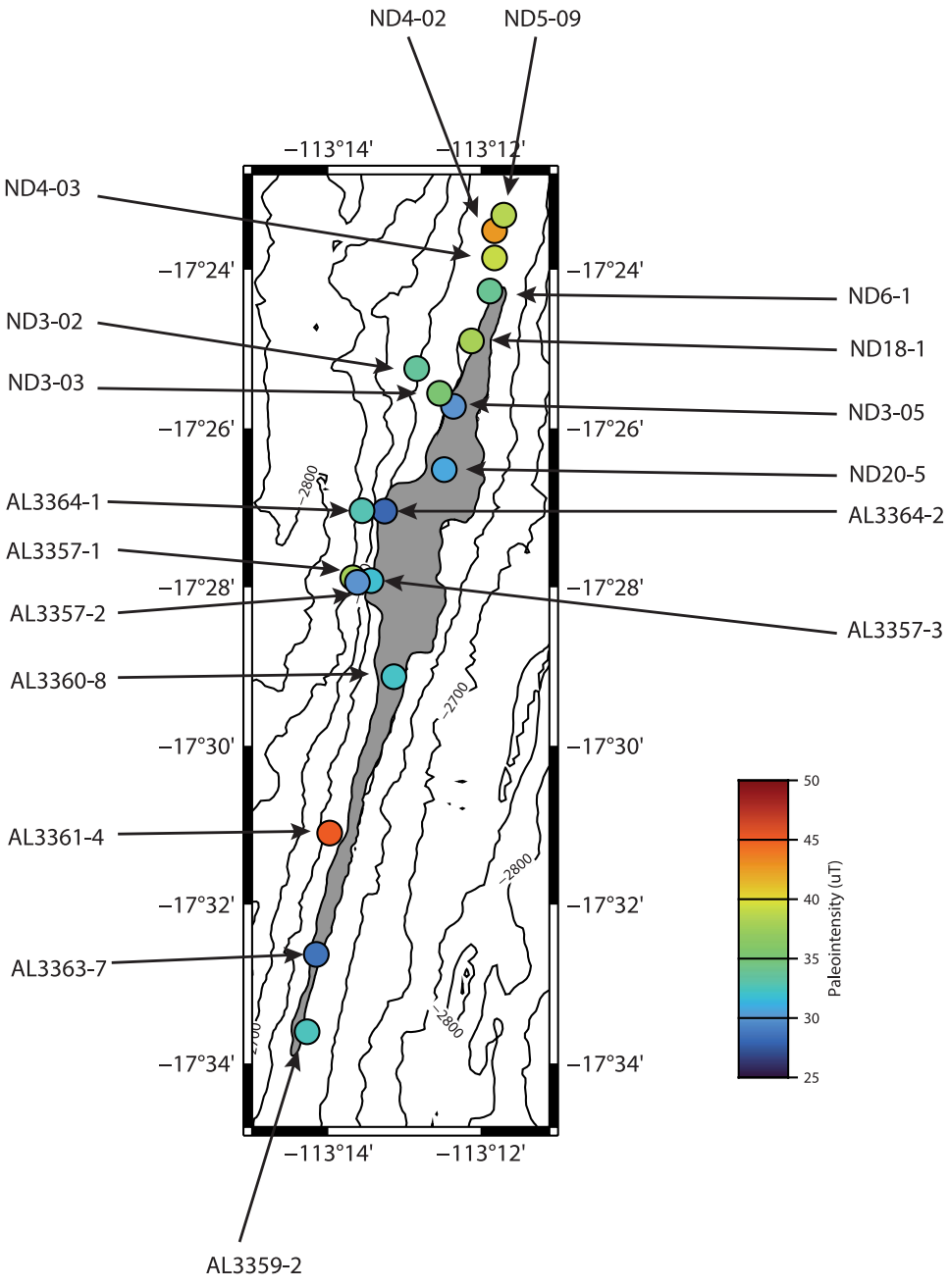

Figure 18: Site paleointensities in the 17°S region.

Flows in the 18°S region are harder to differentiate due to overlapping sample and flow mean paleointensities. In this region, Sinton et al. (2002) identified three flow fields based on dive observations. From oldest to youngest, these are Next Oldest, Animal Farm, and Buddha. With two exceptions (Samples AL3344-4 and AL3345-7), sample mean paleointensities are between 27 and 39 μT (Figure 15). Mean paleointensities for each flow field are within 1 μT of each other. Sinton et al. (2002) estimated that Animal Farm and the Next Oldest flow were most likely emplaced within a few years to decades of each other, and this is supported by the near-identical mean paleointensities for each flow field. Higher sediment contrasts between Buddha and Animal Farm imply a larger recurrence interval than between Next Oldest and Animal Farm; however, the three flows were still emplaced close in time and the resolution of paleointensity likely cannot distinguish the exact degree of difference between decadal-scale intervals, such as these (Sinton et al., 2002).

Samples AL3344-4 and AL3345-7, located by Sinton et al. (2002) within Animal Farm, exhibit high paleointensities of 47.6 and 48.9 μT. The paleointensities are incongruous with the other Animal Farm samples and are located on the edge of the Animal Farm flow boundary suggesting they could belong to a much older flow in the area. The high paleointensities would also separate this unidentified flow from the Next Oldest flow as they indicate an even older emplacement age (Figure 16).

It is interesting to note that the geochemistry from these presumably older outliers more closely resembles that of the younger Animal Farm and the Buddha flows, as opposed to the higher Mg# of the Next Oldest. (Geochemical parameters are plotted against paleointensity-derived emplacement date estimate in Appendix C). If these samples truly represent an older flow, this change in composition could reflect changes in mantle or melting processes. The

relatively low Mg# in this outlier flow is followed by an increase in the Next Oldest flow. The Mg# then returned to the previous lower values for Animal Farm and Buddha within a span of ~50-100 years. If the field models (Figure 2) are correct, the possible outlier flow could have been emplaced several hundred to about two thousand years ago. The fact that dive observations categorized these outlier samples with Animal Farm samples (Sinton et al., 2002) imply a similar degree of sedimentation that would be associated with similar emplacement dates. It could be that the outlier samples were emplaced in between Next Oldest and Animal Farm and the composition was caused by the same event that resulted in the composition of Animal Farm and Buddha. The original combined categorization indicates the outlier samples and Animal Farm were probably emplaced during a similar time period and the field models may not be accurate in this region.

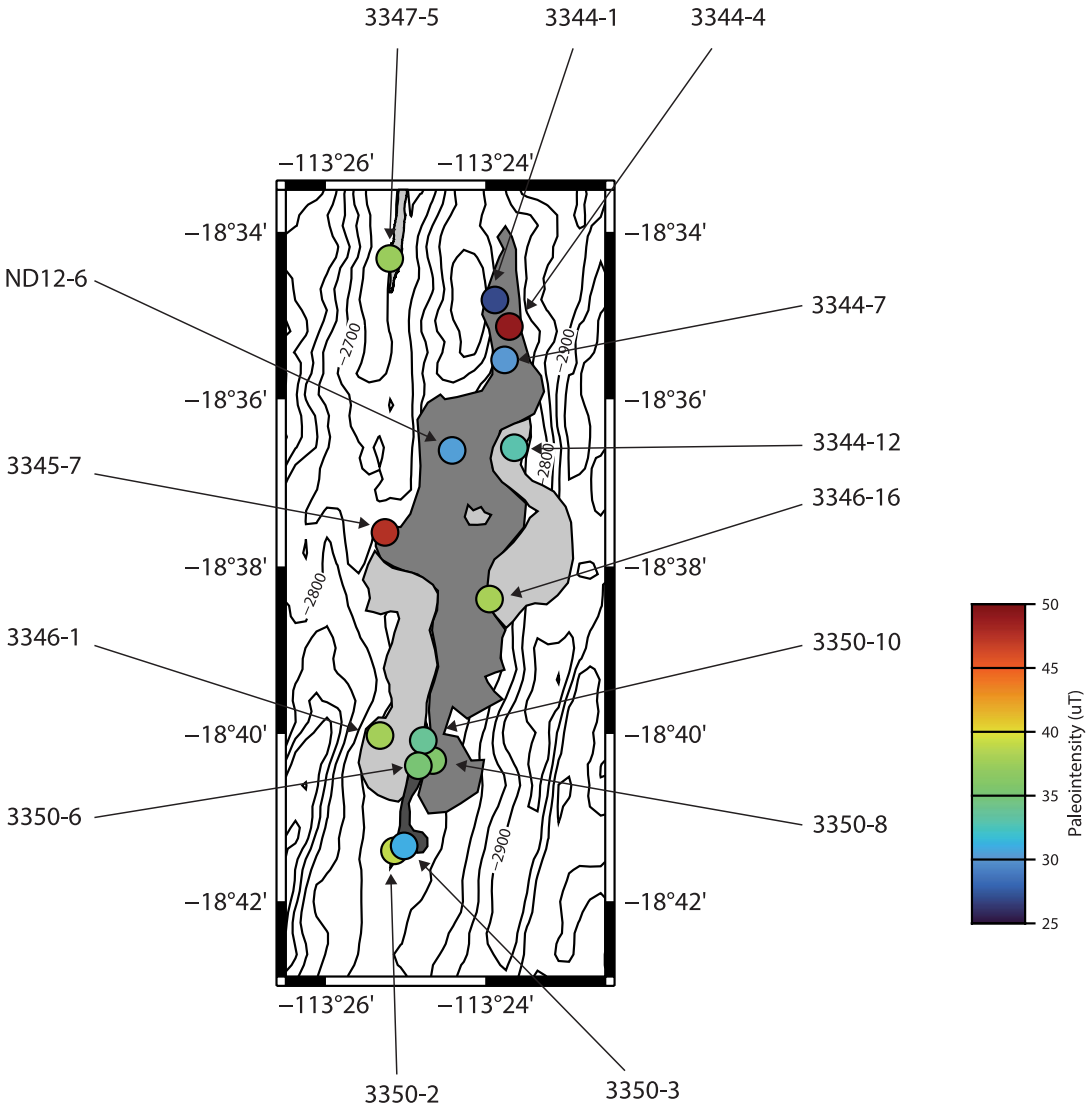

Figure 19: Site paleointensities in the 19°S region.

Relatively close emplacement ages are not surprising in the 17°S and 18°S regions as frequent eruptive activity is thought to occur on the SEPR. At 17°S, recurrence intervals seem to be ~100 years except for Neither B and Aldo-Kihi which are only a few decades apart. At 18°S, eruptions appear to occur within 20-30 years of each other, agreeing with previous estimates from Sinton et al. (2002). These decadal recurrence intervals seem to represent the lower bounds of paleointensity resolution. At both 17°S and 18°S, standard deviations for sample-level paleointensities result in an average emplacement estimate error of ~30 years (according to the HFM model).

We can compare these recurrence interval estimates to the more heavily-studied area at ~9°50'N. There, Po-disequilibrium dating, CO_2 concentrations in basalt glass, and monitoring of hydrothermal vent temperatures allowed for dating the 2005-2006 eruption at 9°N following a 1991-1992 eruption which indicates a recurrence interval of 13 years (Rubin et al., 2006, 2008; Cowen et al., 2007; Barreyre et al., 2022). Assuming this segment experiences a linear, long-term inflation, the next eruption is projected to occur in 2026, giving a recurrence interval of 20 years (Nooner et al., 2014). Along-axis paleointensity data from the same region suggests about a ~150 year age contrast between these recent eruptions and the next oldest flow field (Bowles et al., 2006). General trends in recurrence intervals at 17°S and 18°S largely agree with estimates from 9°N. 18°S and 9°N exhibit groups of eruptive episodes occurring withing a few decades of each other (18°S and 9°N), while 17°S shows groups of episodes separated from other groups by a few hundred years. Perhaps this behavior is evidence of active phases with shorter ~10-20 year recurrence intervals and longer recurrence intervals outside of an "active" phase. This interpretation would agree with behavior observed at the Reykjanes Peninsula consisting of episodes of frequent eruptions separated by longer periods of quiescence (Troll et al., 2024).

Uncertainties in absolute ages arise from at least four causes. One cause could be from real, natural variations in the recorded field. If the underlying terrain has its own magnetization, the glass will acquire a net magnetization reflective of the Earth's magnetic field plus the field from the topography. Smooth and flat flows should produce a minimal effect; however, more textured terrain such as pillows or lobes would have a greater effect (Bowles et al., 2005). A second cause could be from "recording errors" where the magnetic mineralogy of the glass is not ideal and/or has altered in nature. A third cause could be from "recovery errors" in the paleointensity experiments likely contribute to experimental uncertainty, which is partially captured by the calculated uncertainty in the best-fit slope of the Arai plot. A fourth cause could be from uncertainty in the magnetic field models used (CALS10k and HFM10k) which is reflected in the fact that they do not always agree with each other (Figure 2). Peaks and troughs in intensity typically align; however, the magnitudes are different, with HFM10k typically resulting in higher intensities over the last 2000 years than CALS10k. Although there is less uncertainty over the past 200 years, these differences make it more difficult to date the possible outlier flow field.

Cluster Analysis

Different flows could have been emplaced around the same time, acquiring a similar paleointensity. To account for such an overlap, a cluster analysis combines the paleointensity data with the compositional data to attempt to objectively group samples into distinct flow fields.

The utility of the cluster analysis becomes clear when we consider the many samples collected near previously identified flow boundaries at 17°S. These near-boundary samples were recategorized by the cluster analysis from separate flow fields into a combined flow field with

Aldo-Kihi samples (Table 5). Seeing as these recategorized samples are located near flow boundaries, it is possible that Aldo-Kihi is larger than observed during dives and extends to these sample sites. Including these three samples, the range of Mg# is expanded lower and K/Ti is expanded higher which could be explained by chemical heterogeneity in Aldo-Kihi samples (Sinton et al., 2002).

Flow fields at 18°S exhibit more multi-field clustering (Table 5) than flow fields at 17°S, likely due to shorter recurrence intervals present at 18°S. Animal Farm and Buddha clustering together could be because they are all samples from a single flow field or it could reflect the similar geochemistry and emplacement timing of the two flow fields (Sinton et. al., 2002). It is interesting to note that Sinton et al. (2002) believed Animal Farm to be closer in age to the (older) Next Oldest flow than to the (younger) Buddha flow. Yet Animal Farm clusters with Buddha, while the Next Oldest clusters separately. This distinction is likely due to the change in composition, possibly indicative of a mantle recharge event (Sinton et al., 2002), which must have happened over a very short time based on the similar paleointensities. AL3346-16 is similar to other Animal Farm samples in Mg# and K/Ti; however, a paleointensity of 38 μT is not similar to any other sample within the flow field and is likely the reason cluster membership probability is lower than 98%.

Animal Farm and the younger South Hump sample (AL3347-5 in Figure 19) cluster together (Table 5); however it seems unlikely for them to belong to the same flow field as they are geographically distinct; however, it is difficult to draw definitive conclusions when only a single sample from this South Hump flow is available. The South Hump flow field is fairly close to Animal Farm (Figure 19); however, it was observed to be confined within a graben and does not extend to the location of Animal Farm. Additionally, a sample from the northern Lava Shield

flow field around 18°21'S clusters with the Next Oldest samples (Table 5). While the paleointensity and geochemistry between the Lava Shield sample and Next Oldest samples are similar, it seems geographically unlikely that all the samples belonged to the same eruption. The cluster might represent two eruptions happening around the same time fed by magma chambers with a similar composition.

Table 5: Flow field membership before (Sinton et al., 2002) and after cluster analysis recategorization. Only recategorized samples are included. The majority of samples were not recategorized.

Sample	Original Flow Field	Recategorized Flow Field
	17°S	
3357-2	Neither B	Aldo-Kihi
3364-1	Neither B	Aldo-Kihi
ND6-1	17°S Outflow	Aldo-Kihi
AL3359-2	17°S Outflow	Aldo-Kihi
	18°S	
AL3350-10	Buddha	Animal Farm
AL3350-2	Buddha	Animal Farm
AL3350-3	Buddha	Animal Farm
AL3350-6	Buddha	Animal Farm
AL3353-7	Lava Shield	Next Oldest
AL3345-7	Animal Farm	Unidentified Flow Field
AL3344-4	Animal Farm	Unidentified Flow Field
AL3348-5	N South Hump	Unidentified Flow Field

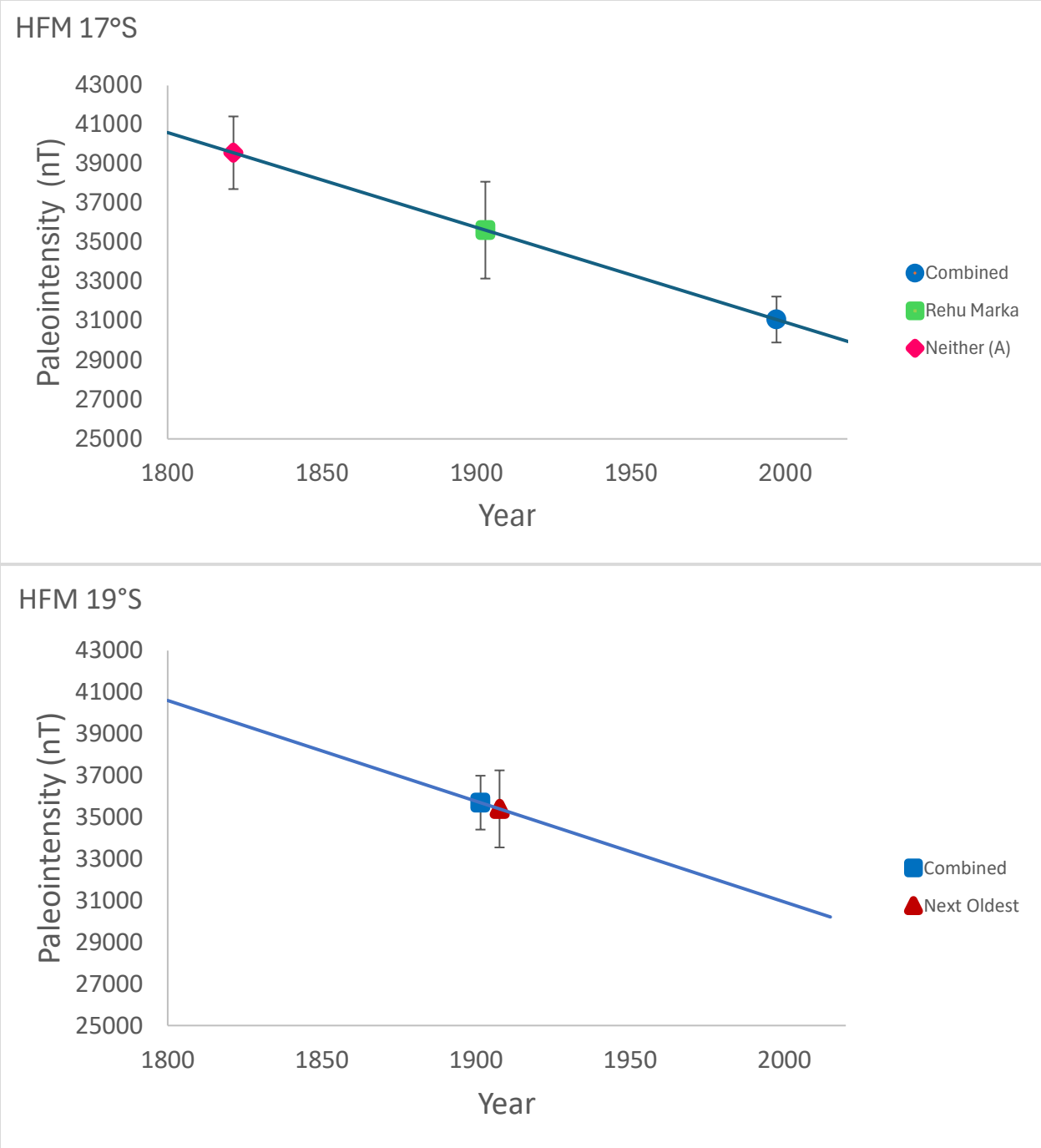

Figure 20: Flow field mean paleointensities as categorized by cluster analysis and corresponding emplacement ages determined from HFM field models (Figure 2) evaluated at 17°S and 19°S (Constable et. al., 2016).

Combining Aldo-Kihi and Neither B samples as well as Buddha and Animal Farm samples based on the cluster analysis results in a slight change in recurrence intervals, but not by much. At 17°S, the recurrence intervals are still ~100 years without the shorter time period between Aldo-Kihi and Neither B that were combined into one emplacement age. At 18°S, the combined Animal Farm and Buddha flow field is indistinguishable from Next Oldest due to the limits of paleointensity resolution; however, it can be extrapolated that the recurrence interval would be less than a few decades (Figure 20). Samples recategorized together by the cluster analysis already had similar paleointensities, so differences in emplacement age and recurrence intervals are minimal.

Samples AL3344-4 and AL3345-5 are recategorized by the cluster analysis to be in a separate, unidentified flow instead of within the Animal Farm flow field. This new flow field is difficult to date as the field models used do not provide an emplacement year for the resulting flow field mean paleointensity. The high mean paleointensity (48.25 μT) suggests emplacement occurred at least a few hundred years ago, which would be a substantial increase in the range of recurrence intervals (originally a few decades) at 18°S.

Statistical Analysis of Paleointensity Variability

One of the original goals of this project was to characterize the natural within-flow field variability in measured paleointensity, and to determine how many samples are required to adequately represent this variability. We could also assess how many samples are required to statistically distinguish between two flow fields with a 1 μT (for example) difference in paleointensity; however, the limited number of glass samples available for this project may be too few to draw meaningful conclusions about internal flow variability.

Table 6: P-values of t-tests comparing mean paleointensities from two flow fields and total number of samples between them. Values in green indicate statistically different means. Values in red do not.

Flow Relationship	Total Samples	p-value
Aldo-Kihi vs Rehu Marka	9	0.00462
Aldo-Kihi vs Neither A	10	0.0000588
Aldo-Kihi vs Neither B	8	0.455
Rehu Marka vs Neither A	7	0.0645
Rehu Marka vs Neither B	5	0.119
Neither A vs Neither B	6	0.0112
Animal Farm vs Buddha	14	0.622
Animal Farm vs Next Oldest	17	0.850
Buddha vs Next Oldest	6	0.825

The mean paleointensity of most previously defined flow fields in both the 17°S and 18°S regions are not statistically different. A two-sample t-test shows p-values greater than 0.05 for most flow field relationships. These p-values indicate the variation between these flow fields could be due to random chance, and we cannot reject the null hypothesis that the data are drawn from the same distribution (e.g., the same flow field). For flow field relationships with a p-value less than 0.05, the paleointensities are statistically distinct at the 95% confidence level, and thus could indicate two different flow fields (Table 6). It is important to note that a high p-value does not mean the paleointensities are statistically similar, just that it cannot be said that they are distinct. Thus, the exact nature of flow field relationships with high p-values is still unknown. Because the t-test is sensitive to sample size, it functions as a starting point but does not provide conclusive results for a majority of flows. A power analysis can be done to determine the number of samples required when designing a project; however, SEPR was chosen as a study site due to a lack of data from the area so this analysis should be used to inform future studies. Additionally, submarine samples are relatively difficult to acquire so sample sizes may not be entirely within our control.

Aside from Aldo-Kihi and Animal Farm, flows only contain 2-3 sample paleointensities, which implies a low statistical power, or a high chance of returning a false negative (Type II error) (Cohen, 1970; Rossi, 1990). A low power also increases the chance of a false positive (Type I error), which should be minimized. An *a priori* power analysis can be conducted to determine how many samples would be needed to ensure sufficient statistical power. A function of this analysis is the effect size, which quantifies the magnitude of the difference between two groups, in this case, flow paleointensities. A large effect size would reflect large differences in paleointensities between two flows, implying they were emplaced at different times. A low effect would represent similar paleointensities and emplacement dates. The Cohen's *d* effect size is calculated for each flow relationship and used to perform the power analysis. Setting the Type I error probability to 0.05 allows for analysis of acceptable sample size for a range of powers (Figure 21).

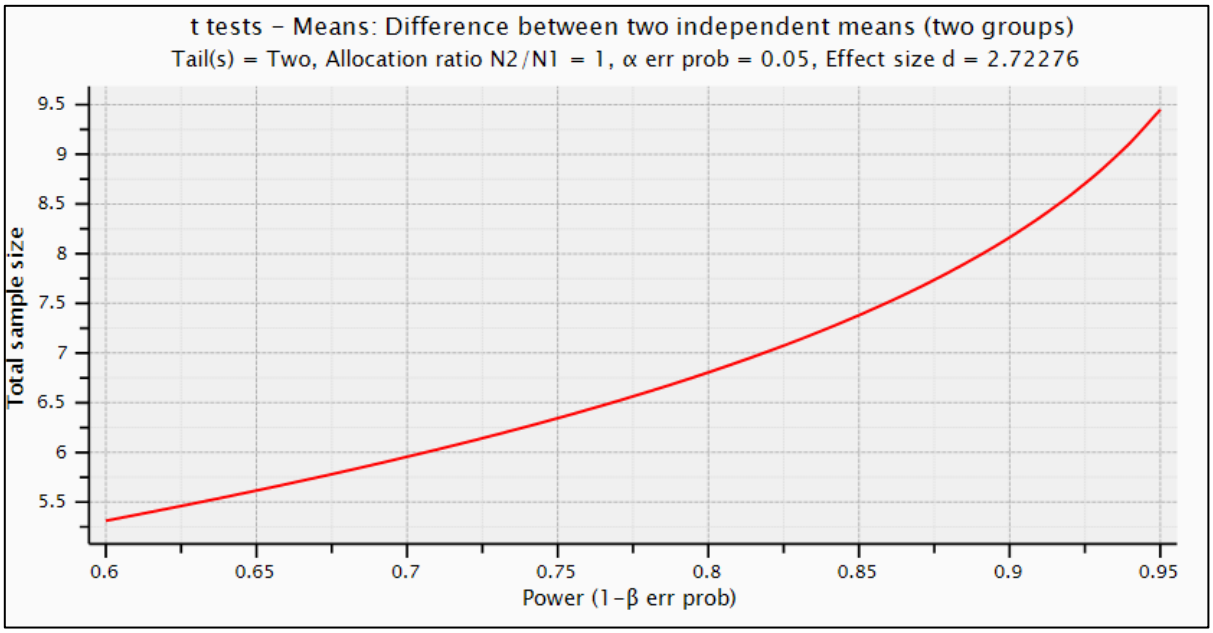

Figure 21: Example a priori power analysis comparing Aldo-Kihi and Rehu Marka. A power of 0.8 would require 7 total samples between the two flow fields. A power of 0.9 would require 8 total samples.

The *a priori* power analysis was used to determine the total number of samples needed to detect a statistical difference between the paleointensities of two flows with a sufficiently powerful dataset. The number of samples varies by region with less samples required at 17°S and more samples required at 18°S. This makes sense because at 17°S, the flows appear to be more differentiated in age (and paleointensity) and thus there is a larger effect size. Six to 16 total samples were required to compare two flows at 17°S depending on the specific flows being compared. Paleointensity means closer together require more samples to differentiate them. It follows that flows in the 18°S region, thought to have been emplaced very close together, required a much higher number of samples to have adequate power. Necessary sample sizes vary from 18 to more than 7000, which would not be a reasonable expectation for an experiment. This trend reflects the limits of the resolution of paleointensity, as the flows in this area are thought to have erupted as close as a few years or decades within each other (Sinton et al., 2002).

If samples from Animal Farm are recategorized in accordance with the cluster analysis instead of dive observations, two outlier samples (AL3357-2 and AL3364-1) are determined to be statistically distinct from Animal Farm, Buddha, and Next Oldest. This result supports the interpretation that these two samples belong to an unidentified flow and not to Animal Farm, as seen in the cluster analysis. Six total samples were necessary to distinguish this new flow field from Animal Farm, Buddha, and Next Oldest.

Recategorizing flow fields in this way resulted in a lower mean paleointensity for Animal Farm and lowers the necessary sample size to differentiate it from other flow fields. Distinguishing it from Buddha still requires a large samples size (90-120) but is lower compared to the previous sizes (700-1000). Distinguishing it from Next Oldest also requires a lower sample size, from the previous 1000s to 26-36.

Based on the power analysis and our prior knowledge of relative age relationships, 7 or 8 samples per flow field should provide a robust data set to accurately determine statistical significance between emplacements on the scale of hundreds of years, such as those seen within the 17°S region. Flow fields emplaced closer together would naturally require a higher number of samples. Based on flow fields at 18°S likely emplaced over ~50 years (Figure 13), a range of 14-16 samples per flow should be adequate. Because this type of paleointensity study requires sample collection via submersible, it may be difficult to reach this threshold for remote areas like SEPR compared to a well-studied and more easily accessed site such as 9°N. However, during dive planning, prior knowledge about relative age relationships should be used to determine the target sample size, with flows emplaced close in time requiring a higher number of samples and vice-versa.

An additional post-hoc power analysis was completed to find the actual power of each flow relationship in an effort to determine if the statistical significance was affected by the low sample size, possibly producing false positives or negatives (Figure 22). The three flow relationships determined to be statistically distinct were also the only relationships to have adequate statistical power. These flows also met or exceeded the required number of samples determined from the a priori power analysis. After recategorization, statistically distinct relationships including the unidentified flow displayed enough power to be reliable. Conventionally, a power of 0.8 and above are considered satisfactory and the flow relationships exhibit powers of 0.90 to 0.99.

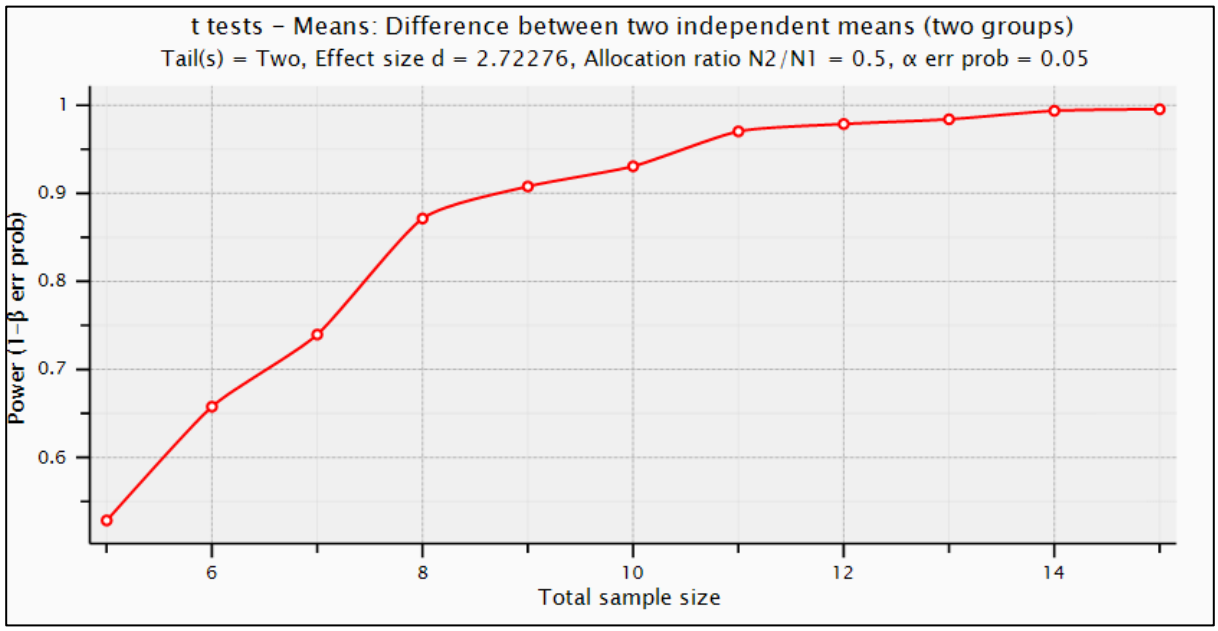

Figure 22: Example post-hoc analysis comparing Aldo-Kihi and Rehu Marka. There are nine total samples between these flows, providing a statistical power is ~0.9 for the dataset.

All the other flow field relationships with high p-values (Table 6) were determined to lack sufficient power with values ranging from 0.05 to 0.48, including relationships involving the recategorized Animal Farm paleointensity. Thus, the flow field relationships with statistical significance are likely representative of a true difference and not a Type I error while the flow field relationships without significance would require larger sample sizes to distinguish the high p-value from a Type II error. It is unsurprising that the 18°S region had the least statistical power because even though the flow fields had more samples available overall, the paleointensities are much closer together and any statistical difference would be on a smaller scale compared to the 17°S results.

At 17°S, samples outside of Aldo-Kihi and Rehu Marka were categorized into two separate flow fields based on geochemistry (Sinton et al., 2002) implying Neither A samples belong to one flow field and Neither B samples belong to a separate flow field when this is not necessarily the case. It would be possible for all samples to belong to the same flow field or have

more than two flow fields represented; however, in this case, paleointensity data and statistical analysis seem to support the idea of two flow fields as previously categorized. Power analyses reveal distinct paleointensities, supporting the interpretation that the eruptions occurred at different times and could be two separate flow fields. Neither B and Aldo-Kihi could potentially belong to the same flow field as their paleointensities are so close together that to reach sufficient power, more than 80 samples would be needed when other relationships in this region need 10-15. Because the power is not sufficient for this experiment, we cannot make definitive conclusions; however, they likely erupted around the same timeframe.

The lack of statistical distinction between Aldo-Kihi and Neither B paleointensities could explain the combined flow field cluster (Figure 17). If the samples truly represent separate flow fields, they could still cluster together based on the low statistical power exhibited by non-Animal Farm samples. Additionally, the statistical power comparing Animal Farm and Buddha paleointensity was quite low (Table 3) so the shared cluster could also be related to the sample size being too low to differentiate them. In either case, it is possible the flow fields would be clustered differently if adequate power was reached with more samples as flow fields comparisons determined to be sufficiently powerful and statistically distinct do not cluster together. For example, Aldo-Kihi and Rehu Marka are statically distinct and form separate clusters. Neither A is statistically distinct from Aldo-Kihi and Neither B while also clustering separately from their combined cluster. Regardless, the fact that two flow fields may cluster together implies that they are closely associated in time.

Conclusion

Distinguishing SEPR flow fields via paleointensity alone is problematic as flow fields emplaced within a relatively short time frame, such as at 18°S, can have overlapping paleointensities. This work tested the application of a GMM cluster analysis in determining boundaries of SEPR flow fields using geochemistry and paleointensity. Paleointensity can function as a temporal constraint to separate flow fields with similar geochemistry, while geochemistry can provide a method of separating flow fields with similar paleointensities. This work was conducted on samples from flow fields with previously defined boundaries to determine the feasibility of this method in regions with unknown boundaries.

At 17°S, paleointensity predicts flow field emplacement dates from 1807 to 2016 with recurrence intervals of ~100 years, except for one interval of a few decades. 18°S flow field paleointensities suggest emplacement dates between 1886 and 1921 with recurrence intervals of a few decades. Paleointensity also allowed for flow field boundaries to be refined. Samples from just outside a flow field but with similar paleointensities to within-field samples may indicate the flow field is larger than originally thought. Conversely, some samples previously identified as part of the same flow field had much higher paleointensities than the majority and could represent a separate flow field.

A GMM cluster approach where the number of clusters is determined using the Bayesian information criterion produces clusters that agree with previously defined flow field boundaries with two notable exceptions. In these two cases, discrete flows cluster together, suggesting that they were emplaced close together in time (less than a few decades). Additionally, a potentially older flow field was identified in Animal Farm samples with paleointensities suggesting a much older emplacement age. This flow field is likely at

least a few hundred years old, but uncertainty in field models makes it difficult to be more precise.

A statistical analysis found that distinguishing between two flow fields based on paleointensity alone required an increasing number of samples for flows separated by less time. At the SEPR, where flow fields have very similar paleointensities and geochemistry, 7 or 8 samples would be enough to differentiate flow fields with recurrence intervals of ~100 years, while twice that amount would be necessary for intervals of a few decades. Decadal-scale recurrence intervals approach the limits of paleointensity resolution and appear to agree with intervals of 13 and 20 years at 9°N (Rubin et al., 2006, 2008; Cowen et al., 2007; Nooner et al., 2014; Barreyre et al., 2022). Flow fields with statistically distinct paleointensities clustered separately. The majority of flow fields did not have sufficient power, but some were clustered separately due to differences in geochemistry. Clusters combining two flow fields also did not have enough samples to reach adequate power which may be the reason for the combined flow fields.

Combining spatial variations in paleointensity and geochemistry in a GMM cluster analysis can be a useful tool in differentiating SEPR flows; however, it should be used in conjunction with dive observations to most accurately draw flow boundaries. Some samples clustered together are geographically distinct, likely indicating separate flow fields. Best practice would be to combine cluster results with dive observations in order to delineate flow boundaries. Future work could explore adding dive observations as another parameter for the cluster analysis to account for geographical constraints on flow field boundaries. For future dive planning, a general idea of recurrence intervals (if known) should be

considered to ensure necessary sample sizes to statistically distinguish flows based on paleointensity alone.

References

Auzende, J.M. et al., 1996, Recent tectonic, magmatic, and hydrothermal activity on the East Pacific Rise between 17°S and 19°S: Submersible observations: Journal of Geophysical Research: Solid Earth, v. 101, p. 17995–18010, doi:10.1029/96JB01209.

Barreyre, T., Parnell-Turner, R., Wu, J.N., and Fornari, D.J., 2022, Tracking Crustal Permeability and Hydrothermal Response During Seafloor Eruptions at the East Pacific Rise, 9°50'N: Geophysical Research Letters, v. 49, p. e2021GL095459, doi:10.1029/2021GL095459.

Bergmanis, E., 1999, Anatomy of a mid-ocean ridge volcanic eruption : The Aldo-Kihi flow between 17°24'S and 17°34'S, East Pacific Rise: Eos Trans. AGU, v. 80, p. F1075, https://cir.nii.ac.jp/crid/1570291225295101824.bib?lang=en (accessed May 2025).

Bergmanis, E.C., Sinton, J., Rubin, K.H., Bergmanis, E.C., Sinton, J., Rubin, K.H., Teagle, D.A.H., and Wilson, D., 2007, Recent eruptive history and magma reservoir dynamics on the southern East Pacific Rise at 17°30′S: Geochemistry, Geophysics, Geosystems, v. 8, p. 12–18, doi:10.1029/2007GC001742.

Bowles, J.A., Colman, A., McClinton, J.T., Sinton, J.M., White, S.M., and Rubin, K.H., 2014, Eruptive timing and 200 year episodicity at 92°W on the hot spot-influenced Galapagos Spreading Center derived from geomagnetic paleointensity: Geochemistry, Geophysics, Geosystems, v. 15, p. 2211–2224, doi:10.1002/2014GC005315.

Bowles, J.A., Gee, J.S., Burgess, K., Cooper, R.F., Bowles, J.A., Gee, J.S., Burgess, K., and Cooper, R.F., 2011, Timing of magnetite formation in basaltic glass: Insights from synthetic analogs and relevance for geomagnetic paleointensity analyses: Geochemistry, Geophysics, Geosystems, v. 12, p. 2001, doi:10.1029/2010GC003404.

Bowles, J., Gee, J.S., Kent, D. V, Bergmanis, E., Sinton, J., Bowles, J., Gee, J.S., Kent, D. V, Bergmanis, E., and Sinton, J., 2005, Cooling rate effects on paleointensity estimates in submarine basaltic glass and implications for dating young flows: Geochemistry, Geophysics, Geosystems, v. 6, p. 7002, doi:10.1029/2004GC000900.

Bowles, J., Gee, J.S., Kent, D. V., Perfit, M.R., Soule, S.A., and Fornari, D.J., 2006, Paleointensity applications to timing and extent of eruptive activity, 9°–10°N East Pacific Rise: Geochemistry, Geophysics, Geosystems, v. 7, doi:10.1029/2005GC001141.

Cann, J.R., Smith, D.K., Cann, J.R., and Smith, D.K., 2005, Evolution of volcanism and faulting in a segment of the Mid-Atlantic Ridge at 25°N: Geochemistry, Geophysics, Geosystems, v. 6, p. 9008, doi:10.1029/2005GC000954.

Carlut, J., and Kent, D. V., 2000, Paleointensity record in zero-age submarine basalt glasses: testing a new dating technique for recent MORBs: Earth and Planetary Science Letters, v. 183, p. 389–401, doi:10.1016/S0012-821X(00)00291-0.

Chadwick, W.W., Paduan, J.B., Clague, D.A., Dreyer, B.M., Merle, S.G., Bobbitt, A.M., Caress, D.W., Philip, B.T., Kelley, D.S., and Nooner, S.L., 2016, Voluminous eruption from a zoned magma body after an increase in supply rate at Axial Seamount: Geophysical Research Letters, v. 43, p. 12,063-12,070, doi:10.1002/2016GL071327.

Clague, D.A. et al., 2013, Geologic history of the summit of Axial Seamount, Juan de Fuca Ridge: Geochemistry, Geophysics, Geosystems, v. 14, p. 4403–4443, doi:10.1002/GGGE.20240.

Coe, R.S., 1967, The determination of paleo-intensities of the Earth's magnetic field with emphasis on mechanisms which could cause non-ideal behavior in Thellier's method: Journal of Geomagnetism and Geoelectricity, v. 19, p. 157–179.

Coe, R.S., Grommé, S., and Mankinen, E.A., 1978, Geomagnetic paleointensities from radiocarbon-dated lava flows on Hawaii and the question of the Pacific nondipole low: Journal of Geophysical Research: Solid Earth, v. 83, p. 1740–1756, doi:10.1029/JB083IB04P01740.

Cohen, J., 1970, Approximate Power and Sample Size Determination for Common one-Sample and two-Sample Hypothesis Tests: Educational and Psychological Measurement, v. 30, p. 811–831, doi:10.1177/001316447003000404.

Constable, C., Korte, M., and Panovska, S., 2016, Persistent high paleosecular variation activity in southern hemisphere for at least 10 000 years: Earth and Planetary Science Letters, v. 453, p. 78–86, doi:10.1016/J.EPSL.2016.08.015.

Cormier, M.H., and Macdonald, K.C., 1994, East Pacific Rise 18°–19°S: Asymmetric spreading and ridge reorientation by ultrafast migration of axial discontinuities: Journal of Geophysical Research: Solid Earth, v. 99, p. 543–564, doi:10.1029/93JB02382.

Cowen, J.P. et al., 2007, Volcanic eruptions at East Pacific Rise near 9°50′N: Eos, Transactions American Geophysical Union, v. 88, p. 81–83, doi:10.1029/2007EO070001.

Dodson, M.H., and McLelland-Brown, E., 1980, Magnetic blocking temperatures of single-domain grains during slow cooling: Journal of Geophysical Research: Solid Earth, v. 85, p. 2625–2637, doi:10.1029/JB085IB05P02625.

Figueiredo, M.A.T., and Jain, A.K., 2002, Unsupervised learning of finite mixture models: IEEE Transactions on Pattern Analysis and Machine Intelligence, v. 24, p. 381–396, doi:10.1109/34.990138.

Gee, J.S., Cande, S.C., Hildebrand, J.A., Donnelly, K., and Parker, R.L., 2000, Geomagnetic intensity variations over the past 780 kyr obtained from near-seafloor magnetic anomalies: Nature, v. 408, p. 827–832, doi:10.1038/35048513.

Goss, A.R., Perfit, M.R., Ridley, W.I., Rubin, K.H., Kamenov, G.D., Soule, S.A., Fundis, A., and Fornari, D.J., 2010, Geochemistry of lavas from the 2005–2006 eruption at the

East Pacific Rise, 9°46′N–9°56′N: Implications for ridge crest plumbing and decadal changes in magma chamber compositions: Geochemistry, Geophysics, Geosystems, v. 11, doi:10.1029/2009GC002977.

Halgedahl, S.L., Day, R., and Fuller, M., 1980, The effect of cooling rate on the intensity of weak-field TRM in single-domain magnetite: Journal of Geophysical Research: Solid Earth, v. 85, p. 3690–3698, doi:10.1029/JB085IB07P03690.

Jackson, A., Jonkers, A.R.T., and Walker, M.R., 2000, Four centuries of geomagnetic secular variation from historical records: Philosophical Transactions of the Royal Society of London. Series A: Mathematical, Physical and Engineering Sciences, v. 358, p. 957–990, doi:10.1098/RSTA.2000.0569.

Kirschvink, J.L., 1980, The least-squares line and plane and the analysis of palaeomagnetic data: Geophysical Journal of the Royal Astronomical Society, v. 62, p. 699–718, doi:10.1111/J.1365-246X.1980.TB02601.X.

Nagata, T., Arai, Y., and Momose, K., 1963, Secular Variation of the Geomagnetic Total Force during the Last 5000 Years: Journal of Geophysical Research, v. 68, p. 5277–5281, doi:10.1029/J.2156-2202.1963.TB00005.X.

Nooner, S.L., Webb, S.C., Buck, W.R., and Cormier, M.H., 2014, Post Eruption inflation of the East Pacific Rise at 9°50′ N: Geochemistry, Geophysics, Geosystems, v. 15, p. 2676–2688, doi:10.1002/2014GC005389.

Paterson, G.A., Biggin, A.J., Yamamoto, Y., and Pan, Y., 2012, Towards the robust selection of Thellier-type paleointensity data: The influence of experimental noise: Geochemistry, Geophysics, Geosystems, v. 13, doi:10.1029/2012GC004046.

Paterson, G.A., Tauxe, L., Biggin, A.J., Shaar, R., and Jonestrask, L.C., 2014, On improving the selection of Thellier-type paleointensity data: Geochemistry, Geophysics, Geosystems, v. 15, p. 1180–1192, doi:10.1002/2013GC005135.

Pick, T., and Tauxe, L., 1993, Holocene paleointensities: Thellier Experiments on submarine basaltic glass from the East Pacific Rise: Journal of Geophysical Research: Solid Earth, v. 98, p. 17949–17964, doi:10.1029/93JB01160.

Rossi, J.S., 1990, Statistical power of psychological research: What have we gained in 20 years? Journal of Consulting and Clinical Psychology, v. 58, p. 646–656, doi:10.1037/0022-006X.58.5.646.

Rubin, K.H. et al., 2006, Geochronology and Composition of the 2005-06 Volcanic Eruptions of the East Pacific Rise, 9° 46’-56’N, Abstract V23B-0602, Fall Meeting of the American Geophysical Union, San Francisco.

Rubin, K.H. et al., 2008, Integrating Radiometric, Geophysical and Thermal Signals of Volcanic Unrest and Eruption in 2005-06 at 9°50’N EPR, Abstract B23F-07, Fall Meeting of the American Geophysical Union, San Francisco.

Rubin, K.H., Smith, M.C., Bergmanis, E.C., Perfit, M.R., Sinton, J.M., and Batiza, R., 2001, Geochemical heterogeneity within mid-ocean ridge lava flows: insights into eruption, emplacement and global variations in magma generation: Earth and Planetary Science Letters, v. 188, p. 349–367, doi:10.1016/S0012-821X(01)00339-9.

Sadeghi, B., 2025, Clustering in geo-data science: Navigating uncertainty to select the most reliable method: Ore Geology Reviews, v. 181, p. 106591, doi:10.1016/J.OREGEOREV.2025.106591.

Selkin, P.A., Gee, J.S., Tauxe, L., Meurer, W.P., and Newell, A.J., 2000, The effect of remanence anisotropy on paleointensity estimates: a case study from the Archean Stillwater Complex: Earth and Planetary Science Letters, v. 183, p. 403–416, doi:10.1016/S0012-821X(00)00292-2.

Shaar, R., and Tauxe, L., 2013, Thellier GUI: An integrated tool for analyzing paleointensity data from Thellier-type experiments: Geochemistry, Geophysics, Geosystems, v. 14, p. 677–692, doi:10.1002/GGGE.20062.

Sinton, J., Bergmanis, E., Rubin, K., Batiza, R., Gregg, T.K.P., Grönvold, K., Macdonald, K.C., and White, S.M., 2002, Volcanic eruptions on mid-ocean ridges: New evidence from the superfast spreading East Pacific Rise, 17°–19°S: Journal of Geophysical Research: Solid Earth, v. 107, p. ECV 3-1, doi:10.1029/2000JB000090.

Tanaka, H., and Kobayashi, T., 2003, Paleomagnetism of the late Quaternary Ontake Volcano, Japan: Directions, intensities, and excursions: Earth, Planets and Space, v. 55, p. 189–202, doi:10.1186/BF03351748/METRICS.

Tauxe, L, Banerjee, S.K., Butler, R.F. and van der Voo R, 2018, Essentials of Paleomagnetism, 5th Web Edition.

Tauxe, L., Shaar, R., Jonestrask, L., Swanson-Hysell, N.L., Minnett, R., Koppers, A.A.P., Constable, C.G., Jarboe, N., Gaastra, K., and Fairchild, L., 2016, PmagPy: Software package for paleomagnetic data analysis and a bridge to the Magnetics Information Consortium (MagIC) Database: Geochemistry, Geophysics, Geosystems, v. 17, p. 2450–2463, doi:10.1002/2016GC006307/.

Tauxe, L., and Staudigel, H., 2004, Strength of the geomagnetic field in the Cretaceous Normal Superchron: New data from submarine basaltic glass of the Troodos Ophiolite: Geochemistry, Geophysics, Geosystems, v. 5, doi:10.1029/2003GC000635.

Tauxe, L., and Yamazaki, T., 2015, Paleointensities: Treatise on Geophysics: Second Edition, v. 5, p. 461–509.

Thellier, E., and Thellier, O., 1959, Sur l'intensité du champ magnétique terrestre dans le passé historique et géologique: Annales de Geophysique, v. 15, p. 285, https://ui.adsabs.harvard.edu/abs/1959AnG....15..285T/abstract (accessed May 2025).

Troll, V.R., Deegan, F.M., Thordarson, T., Tryggvason, A., Krmíček, L., Moreland, W.M., Lund, B., Bindeman, I.N., Höskuldsson, Á., and Day, J.M.D., 2024, The Fagradalsfjall and Sundhnúkur Fires of 2021–2024: A single magma reservoir under the Reykjanes Peninsula, Iceland? Terra Nova, v. 36, p. 447–456, doi:10.1111/TER.12733.

Waters, C.L., Sims, K.W.W., Soule, S.A., Blichert-Toft, J., Dunbar, N.W., Plank, T., Prytulak, J., Sohn, R.A., and Tivey, M.A., 2013, Recent volcanic accretion at 9°N–10°N East Pacific Rise as resolved by combined geochemical and geological observations: Geochemistry, Geophysics, Geosystems, v. 14, p. 2547–2574, doi:10.1002/GGGE.20134.

Yu, Y., Tauxe, L., and Genevey, A.S., 2004, Toward an optimal geomagnetic field intensity determination technique: Geochem. Geophys. Geosyst, v. 5, p. 2–07, doi:10.1029/2003GC000630.

Zhou, W., Van Der Voo, R., Peacor, D.R., and Zhang, Y., 2000, Variable Ti-content and grain size of titanomagnetite as a function of cooling rate in very young MORB: Earth and Planetary Science Letters, v. 179, p. 9–20, doi.org/10.1016/S0012-821X(00)00100-X.

Appendix A: Specimen Statistics

Table 7: Specimen statistics for 17°S region. [a]

Specimen	Sample	Flow	int_abs	F_{anc}	β	*f*	FRAC	q	SCAT	DANG	MAD_{free}	DRAT	DRATS	Status
V001	ND20-5	Aldo-Kihi	3.08E-05	30.8	0.01	0.98	0.98	102.24	TRUE	1.49	7.16	1.33	2.28	Accepted
V002	ND20-5	Aldo-Kihi	3.08E-05	30.8	0.01	0.9	0.92	66.2	TRUE	2.38	9.88	0.61	0.57	Accepted
V003	ND20-5	Aldo-Kihi	2.88E-05	28.8	0.05	0.83	0.89	15.15	TRUE	8.43	13.12	5.57	5.06	Rejected
V004	ND20-5	Aldo-Kihi	3.18E-05	31.8	0.01	0.94	0.94	66.08	TRUE	3.94	5.82	1.2	1.73	Accepted
V005	ND20-5	Aldo-Kihi	2.97E-05	29.7	0.02	0.89	0.91	31.68	TRUE	5.05	4.4	3.26	7.37	Accepted
V006	AL3357-1	Neither B	3.93E-05	39.3	0.01	0.87	0.86	90.76	TRUE	4.6	8.86	2.21	2.97	Accepted
V007	AL3357-1	Neither B	4.10E-05	41.0	0.04	0.91	0.93	22.82	TRUE	11.25	6.41	9.77	25.88	Rejected
V008	AL3357-1	Neither B	3.70E-05	37.0	0.02	0.91	0.9	34.57	TRUE	5.41	7.35	3.7	10.18	Rejected
V009	AL3357-1	Neither B	4.28E-05	42.8	0.03	0.77	0.78	20.35	TRUE	3.55	7.62	5.84	9.12	Rejected
V010	AL3357-1	Neither B	3.62E-05	36.2	0.03	0.9	0.92	23.88	TRUE	3.05	8.31	5.19	0.64	Accepted
V011	AL3357-2	Neither A	2.91E-05	29.1	0.02	0.83	0.8	33.64	TRUE	1.77	6.93	6.24	4.34	Accepted
V012	AL3357-2	Neither A	3.02E-05	30.2	0.01	0.84	0.81	56.08	TRUE	3.39	5.88	1.56	2.56	Accepted
V013	AL3357-2	Neither A	3.14E-05	31.4	0	0.86	0.75	156.31	TRUE	3.78	8.1	1.46	2.71	Accepted
V014	AL3357-2	Neither A	3.02E-05	30.2	0.01	0.92	0.89	89.19	TRUE	3.69	5.51	0.62	1.83	Accepted
V015	AL3357-2	Neither A	2.90E-05	29.0	0.01	0.93	0.94	121.21	TRUE	2.51	7.6	2.17	5.8	Accepted
V016	AL3357-3	Aldo-Kihi	3.15E-05	31.5	0	0.95	0.95	185.97	TRUE	1.51	4.49	0.48	1.19	Accepted
V017	AL3357-3	Aldo-Kihi	3.25E-05	32.5	0.01	0.89	0.88	61.88	TRUE	2.62	5.81	1.55	2.54	Accepted
V018	AL3357-3	Aldo-Kihi	3.17E-05	31.7	0.01	0.8	0.81	123.99	TRUE	1.86	6.69	0.57	0.96	Accepted
V019	AL3357-3	Aldo-Kihi	3.17E-05	31.7	0.01	0.87	0.86	59.02	TRUE	1.89	6.61	3.79	1.11	Accepted
V020	AL3357-3	Aldo-Kihi	3.22E-05	32.2	0.02	0.91	0.81	50.17	TRUE	0.55	2.1	1.98	4.49	Accepted
V021	AL3364-1	Neither A	3.36E-05	33.6	0.01	0.93	0.95	70.72	TRUE	3.28	7.38	3.82	5.32	Accepted
V022	AL3364-1	Neither A	3.35E-05	33.5	0.02	0.96	0.95	40.85	TRUE	0.76	4.06	1.79	3.66	Accepted
V023	AL3364-1	Neither A	3.10E-05	31.0	0.03	0.81	0.78	24.01	TRUE	3.52	7.88	4.66	4.2	Accepted
V024	AL3364-1	Neither A	3.28E-05	32.8	0.02	0.84	0.86	30.1	TRUE	5.18	7.99	6.27	7.82	Accepted
V025	AL3364-1	Neither A	3.33E-05	33.3	0.02	0.85	0.84	37.42	TRUE	3.68	9.78	3.14	6.06	Accepted
V026	AL3364-2	Aldo-Kihi	2.88E-05	28.8	0.03	0.86	0.83	21.17	TRUE	1.61	10.33	3.92	1.84	Accepted
V027	AL3364-2	Aldo-Kihi	3.07E-05	30.7	0.05	0.84	0.82	15.84	TRUE	4.67	7.78	7.39	8.43	Accepted

Specimen	Sample	Flow	int_abs	F_{anc}	β	*f*	FRAC	q	SCAT	DANG	MAD_{free}	DRAT	DRATS	Status
V029	AL3364-2	Aldo-Kihi	2.47E-05	24.7	0.03	0.81	0.78	20.99	TRUE	3.33	6.33	4.87	1.03	Accepted
V030	AL3365-8	Aldo-Kihi	3.05E-05	30.5	0.07	0.75	0.66	10.15	FALSE	10.43	12.7	15.72	14.7	Rejected
V031	AL3365-8	Aldo-Kihi	1.76E-05	17.6	0.13	0.57	0.45	2.99	TRUE	11.35	32.35	24.49	19.11	Rejected
V032	AL3365-8	Aldo-Kihi	3.73E-05	37.3	0.11	0.73	0.83	5.32	FALSE	17.84	17.28	11.71	0.33	Rejected
V033	AL3365-8	Aldo-Kihi	2.64E-05	26.4	0.05	0.83	0.79	14.67	TRUE	14.27	12.51	17.09	10.31	Rejected
V034	ND3-1	Rehu Marka	1.07E-05	10.7	0.13	0.64	0.29	4.08	TRUE	13.9	16.92	11.42	2.14	Rejected
V035	ND3-1	Rehu Marka	3.55E-05	35.5	0.02	0.72	0.79	37.93	TRUE	8.78	12.12	1.7	2.61	Rejected
V036	ND3-1	Rehu Marka	2.57E-05	25.7	0.02	0.56	0.53	20.92	TRUE	12.52	12.09	3.12	1.64	Rejected
V037	ND3-1	Rehu Marka	1.52E-05	15.2	0.07	0.63	0.45	7.2	TRUE	28.57	17.01	11.12	6.28	Rejected
V038	ND3-2	Rehu Marka	3.04E-05	30.4	0.03	0.92	0.89	28.78	TRUE	4.61	7.92	2.65	0.97	Accepted
V039	ND3-2	Rehu Marka	3.78E-05	37.8	0.04	0.97	0.98	19.47	TRUE	3.67	7.65	3.06	0.08	Accepted
V040	ND3-2	Rehu Marka	3.04E-05	30.4	0.04	0.67	0.58	14.87	TRUE	7.37	9.12	4.02	3.26	Accepted
V041	ND3-2	Rehu Marka	3.44E-05	34.4	0.02	0.99	0.98	39.19	TRUE	7.77	7.5	2.35	0.43	Accepted
V042	ND3-2	Rehu Marka	3.51E-05	35.1	0.02	0.95	0.94	55.64	TRUE	1.86	8.6	1.77	0.67	Accepted
V043	ND3-3	Rehu Marka	3.68E-05	36.8	0.08	0.96	0.91	10.95	FALSE	0.98	10.45	4.87	3.54	Rejected
V044	ND3-3	Rehu Marka	3.29E-05	32.9	0.05	1.01	0.98	18.75	TRUE	2.25	10.15	5.85	3.22	Accepted
V045	ND3-3	Rehu Marka	3.78E-05	37.8	0.03	0.99	0.97	25.45	TRUE	2.59	9.48	2.98	0.15	Accepted
V046	ND4-2	Neither B	4.46E-05	44.6	0.03	0.75	0.87	22.25	TRUE	2.48	6.16	1.08	1.57	Accepted
V047	ND4-2	Neither B	4.05E-05	40.5	0.02	0.83	0.89	41.89	TRUE	2.71	5.36	2.17	1.98	Accepted
V048	ND4-2	Neither B	4.36E-05	43.6	0.02	0.79	0.82	33.33	TRUE	5.58	8.51	3.49	3.37	Accepted
V049	ND4-2	Neither B	4.23E-05	42.3	0.01	0.64	0.74	52.44	TRUE	0.21	1.81	2.91	0.16	Accepted
V050	ND4-2	Neither B	4.25E-05	42.5	0.04	0.67	0.7	16.65	TRUE	1.47	3.7	3.65	0.75	Accepted
V051	ND4-3	Neither A	4.09E-05	40.9	0.01	0.96	0.97	77.21	TRUE	3.11	6.68	3.48	5.78	Accepted
V052	ND4-3	Neither A	3.65E-05	36.5	0.02	0.76	0.64	40.46	TRUE	1.83	7.26	10.84	12.08	Rejected
V053	ND4-3	Neither A	3.96E-05	39.6	0.03	0.93	0.87	25.15	TRUE	4.26	4.24	4.02	7.64	Accepted
V054	ND4-3	Neither A	3.54E-05	35.4	0.01	0.88	0.94	54.96	TRUE	2.53	7.02	5.12	10.25	Rejected
V055	ND4-3	Neither A	3.72E-05	37.2	0.02	0.82	0.88	43.67	TRUE	0.82	4.32	2.41	6.57	Accepted
V056	ND5-9	Neither A	3.68E-05	36.8	0.02	0.87	0.74	43.79	TRUE	2.98	3.39	2.89	3.72	Accepted
V057	ND5-9	Neither A	4.03E-05	40.3	0.01	0.91	0.91	56.94	TRUE	3.83	4.18	2.01	2.19	Accepted
V058	ND5-9	Neither A	4.06E-05	40.6	0.01	0.94	0.95	62.8	TRUE	2.59	4.45	0.89	2.15	Accepted
V059	ND5-9	Neither A	3.68E-05	36.8	0.02	0.76	0.75	33.16	TRUE	1.63	8.41	1.77	1.95	Accepted

Specimen	Sample	Flow	int_abs	F_{anc}	β	*f*	FRAC	q	SCAT	DANG	MAD_{free}	DRAT	DRATS	Status
V060	ND5-9	Neither A	3.87E-05	38.7	0.02	0.79	0.78	40.04	TRUE	3.46	8.05	5.52	8.84	Accepted

Table 8: Specimen statistics for 18°S region. [a]

Specimen	Sample	Flow	int_abs	F_{anc}	β	*f*	FRAC	q	SCAT	DANG	MAD_{free}	DRAT	DRATS	Status
B02161	3350-6	Buddha	3.61E-05	36.1	0.05	0.99	0.97	18.26	TRUE	4.71	8.49	3.96	4.88	Accepted
B02162	3350-6	Buddha	3.48E-05	34.8	0.04	0.87	0.76	21.35	TRUE	3.56	11.1	12.98	9.47	Rejected
B02163	3350-6	Buddha	3.41E-05	34.1	0.07	0.88	0.72	11.36	TRUE	7.08	7.66	5.23	0.59	Accepted
B02164	3345-2	Animal Farm	3.15E-05	31.5	0.02	0.98	0.97	40.77	TRUE	3.73	3.72	2.66	0.4	Accepted
B02166	3345-2	Animal Farm	3.44E-05	34.4	0.04	0.85	0.57	16.21	TRUE	2.89	11.05	8.51	10.13	Accepted
B02168	3350-4	Buddha	1.22E-05	12.2	0.12	0.97	0.83	7.11	FALSE	32.29	12.94	3.09	1.99	Rejected
B02169	3350-4	Buddha	5.47E-06	5.50	0.1	0.92	0.81	7.86	FALSE	46	24.32	4.01	5.95	Rejected
B02170	3350-4	Buddha	1.91E-05	19.1	0.02	0.95	0.98	33.59	TRUE	25.37	20.78	1.58	1.31	Rejected
B02171	3350-4	Buddha	1.14E-05	11.4	0.04	0.91	0.98	18.56	TRUE	45.56	27.43	5.64	6.2	Rejected
B02172	3346-1	Next Oldest	4.18E-05	41.8	0.01	0.93	0.95	119.57	TRUE	3.74	4.14	3.11	4.42	Accepted
B02173	3346-1	Next Oldest	4.44E-05	44.4	0.02	0.91	0.94	49.06	TRUE	1.88	4.3	2.76	0.51	Accepted
B02174	3346-1	Next Oldest	3.97E-05	39.7	0.01	0.89	0.91	110.84	TRUE	1.31	3.64	1.71	3.29	Accepted
B02175	3346-1	Next Oldest	4.31E-05	43.1	0.02	0.96	0.96	49.15	TRUE	2.4	3.43	2.74	7.63	Accepted
B02176	3346-1	Next Oldest	2.02E-05	20.2	0.08	0.72	0.8	7.56	TRUE	22.55	19.74	9.3	24.82	Rejected
B02177	3350-3	Buddha	2.57E-05	25.7	0.06	1.06	0.97	17.39	FALSE	10.25	13.78	184.17	233.78	Rejected
B02178	3350-3	Buddha	3.26E-05	32.6	0.01	0.96	0.96	94.08	TRUE	2.02	3.05	0.26	1.04	Accepted
B02179	3350-3	Buddha	3.41E-05	34.1	0.03	0.78	0.52	24.24	TRUE	4.11	6.14	2.56	1.92	Accepted
B02180	3350-3	Buddha	3.22E-05	32.2	0.02	0.95	0.95	47.13	TRUE	2.11	2.73	2.12	5.86	Accepted
B02181	3350-2	Buddha	3.45E-05	34.5	0.02	0.95	0.97	45	TRUE	0.97	7.89	2.31	1.98	Accepted
B02182	3350-2	Buddha	3.97E-05	39.7	0.04	0.76	0.83	15.51	TRUE	1.93	6.18	3.38	7.33	Accepted
B02183	3350-2	Buddha	3.38E-05	33.8	0.08	0.82	0.92	8.94	FALSE	14.58	12.8	9.8	1.58	Rejected
B02184	3350-2	Buddha	4.80E-05	48.0	0.07	1.04	0.97	12.67	FALSE	9.9	15.37	10.54	8.25	Rejected
B02185	3350-10	Buddha	3.37E-05	33.7	0.04	0.89	0.86	21.01	TRUE	6.2	7.5	7.21	7.98	Accepted
B02186	3350-10	Buddha	3.32E-05	33.2	0.1	0.72	0.43	5.58	TRUE	7.93	15.71	9.09	8.77	Rejected
B02187	3350-10	Buddha	3.30E-05	33.0	0.03	1	0.97	26.06	TRUE	2.25	7.87	3.77	4.36	Accepted
B02188	3350-10	Buddha	3.63E-05	36.3	0.06	0.97	0.98	14.32	FALSE	4.86	12.3	6.6	16.43	Rejected
B02189	3350-10	Buddha	3.27E-05	32.7	0.01	0.85	0.71	58.03	TRUE	5.01	1.78	1.39	1.05	Accepted
B02190	3346-8	Next Oldest	4.80E-06	4.80	0.24	0.38	0.42	1.08	TRUE	56.18	37.26	12.58	3.73	Rejected
B02191	3346-8	Next Oldest	2.67E-05	26.7	0.07	0.97	0.94	11.97	FALSE	12.34	16.08	11.09	11.92	Rejected

Specimen	Sample	Flow	int_abs	F_{anc}	β	*f*	FRAC	q	SCAT	DANG	MAD_{free}	DRAT	DRATS	Status
B02192	3346-8	Next Oldest	5.56E-05	55.6	0.08	0.92	0.73	10.18	FALSE	12.86	9.22	4.54	19.22	Rejected
B02193	3343-10	Animal Farm	3.14E-05	31.4	0.03	0.96	0.95	31.13	TRUE	10.32	5.15	2.35	2.24	Accepted
B02194	3343-10	Animal Farm	3.07E-05	30.7	0.01	0.97	0.98	107.33	TRUE	1.39	3.11	1.25	2.89	Accepted
B02196	3346-3	Next Oldest	3.78E-05	37.8	0.04	0.94	0.79	22.16	TRUE	5.99	5.55	3.93	2.84	Accepted
B02197	3346-3	Next Oldest	4.90E-05	49.0	0.04	0.88	0.93	21.29	TRUE	3.06	2.08	2.28	5.91	Accepted
B02198	3346-3	Next Oldest	4.09E-05	40.9	0.09	0.97	0.76	10.18	FALSE	12.75	19.41	12.13	2.03	Rejected
B02199	3344-1	Animal Farm	2.10E-05	21.0	0.18	1.02	0.89	5.01	FALSE	31.47	22.2	42.79	59.66	Rejected
B02200	3344-1	Animal Farm	3.09E-05	30.9	0.02	0.97	0.98	47.98	TRUE	0.45	4.16	1.05	1.57	Accepted
B02201	3344-1	Animal Farm	2.58E-05	25.8	0.04	0.63	0.76	12.73	TRUE	35.24	10.59	7.58	3.79	Rejected
B02202	3344-1	Animal Farm	3.02E-05	30.2	0.04	0.85	0.54	16.82	TRUE	3.86	9.68	3.16	7.83	Accepted
B02203	3344-12	Next Oldest	3.08E-05	30.8	0.01	0.95	0.94	113.13	TRUE	0.51	3.53	1.34	1.68	Accepted
B02204	3344-12	Next Oldest	3.15E-05	31.5	0.01	0.98	0.96	61.27	TRUE	1.34	2.26	0.81	0.61	Accepted
B02205	3344-12	Next Oldest	3.43E-05	34.3	0.02	0.97	0.95	44.48	TRUE	0.95	3.18	1.06	3.37	Accepted
B02206	3344-12	Next Oldest	3.46E-05	34.6	0.01	0.96	0.96	139.49	TRUE	1.75	3.99	0.73	1.76	Accepted
B02207	3344-12	Next Oldest	3.37E-05	33.7	0.01	0.93	0.95	75.24	TRUE	2.76	4.1	1.19	0.28	Accepted
B02208	3350-8	Animal Farm	3.69E-05	36.9	0.01	0.97	0.98	75.69	TRUE	0.59	2.02	1.01	1.64	Accepted
B02209	3350-8	Animal Farm	3.58E-05	35.8	0.01	0.96	0.96	58.47	TRUE	1.39	3.52	1.78	1.65	Accepted
B02210	3350-8	Animal Farm	3.49E-05	34.9	0.02	0.92	0.94	38.3	TRUE	4.1	4.23	3.69	1.17	Accepted
B02211	3350-8	Animal Farm	3.55E-05	35.5	0.03	0.88	0.89	29.46	TRUE	2.16	3.35	2.26	2.02	Accepted
B02212	3345-8	Animal Farm	2.61E-05	26.1	0.07	0.67	0.68	8.65	TRUE	10.88	6.02	2.97	0.66	Accepted
B02213	3345-8	Animal Farm	1.99E-05	19.9	0.02	0.77	0.75	30.05	TRUE	19.32	10.25	2.73	4.32	Rejected
B02214	3345-8	Animal Farm	2.20E-05	22.0	0.02	0.97	0.95	35.48	TRUE	12	8.24	1.55	3.2	Rejected
B02215	3345-8	Animal Farm	3.22E-05	32.2	0.01	0.98	0.98	92.18	TRUE	1.92	3.43	1.36	3.02	Accepted
B02216	3344-4	Animal Farm	5.23E-05	52.3	0.04	0.9	0.95	20.89	TRUE	3.7	1.89	2.78	18.83	Rejected
B02217	3344-4	Animal Farm	4.82E-05	48.2	0.03	0.9	0.94	28.46	TRUE	3.65	2.29	2.06	10.09	Accepted
B02218	3344-4	Animal Farm	4.85E-05	48.5	0.03	0.87	0.91	28.78	TRUE	2.77	2.62	1.69	8.7	Accepted
B02219	3344-4	Animal Farm	4.74E-05	47.4	0.02	0.86	0.9	32.51	TRUE	2.55	1.28	1.99	7.85	Accepted
B02220	3344-4	Animal Farm	4.82E-05	48.2	0.02	0.89	0.93	36.38	TRUE	2.68	2.71	2.04	12.05	Rejected
B02221	3346-16	Next Oldest	4.03E-05	40.3	0.01	0.96	0.97	59.51	TRUE	1.69	2.01	1.4	6.62	Accepted
B02222	3346-16	Next Oldest	3.02E-05	30.2	0.1	0.85	0.92	6.68	FALSE	3.98	18.77	20.62	8.37	Rejected
B02223	3346-16	Next Oldest	4.34E-05	43.4	0.03	0.92	0.87	30.72	TRUE	2.41	2.81	1.64	4.95	Accepted

Specimen	Sample	Flow	int_abs	F_{anc}	β	*f*	FRAC	q	SCAT	DANG	MAD_{free}	DRAT	DRATS	Status
B02224	3344-7	Animal Farm	3.28E-05	32.8	0.02	0.95	0.95	44.46	TRUE	3.51	4.35	2.42	9.21	Accepted
B02225	3344-7	Animal Farm	2.94E-05	29.4	0.02	0.95	0.93	40.54	TRUE	4.61	3.49	3.48	2.44	Accepted
B02226	3344-7	Animal Farm	2.85E-05	28.5	0.04	0.93	0.9	23.67	TRUE	0.52	3.67	3.31	6.82	Accepted
B02227	ND12-6	Animal Farm	2.82E-05	28.2	0.02	0.91	0.91	41.66	TRUE	5.27	4.63	2.26	4.81	Accepted
B02228	ND12-6	Animal Farm	2.96E-05	29.6	0.04	0.84	0.88	19.66	TRUE	12.59	7.14	4.97	5.67	Rejected
B02229	ND12-6	Animal Farm	3.10E-05	31.0	0.02	0.96	0.95	50.15	TRUE	4.3	3.78	2.05	0.99	Accepted
B02230	ND12-6	Animal Farm	3.26E-05	32.6	0.02	0.93	0.91	45.53	TRUE	3.9	3.6	3.45	1.55	Accepted
B02231	ND12-6	Animal Farm	3.12E-05	31.2	0.02	0.96	0.95	46.95	TRUE	2.78	3.88	1.93	2.37	Accepted
B02232	ND12-5	Animal Farm	2.42E-05	24.2	0.07	0.91	0.77	10.87	FALSE	13.93	13.61	6.76	0.07	Rejected
B02233	ND12-5	Animal Farm	1.64E-05	16.4	0.06	0.56	0.76	9.19	TRUE	27.86	26.94	8.66	11.28	Rejected
B02234	ND12-5	Animal Farm	2.86E-05	28.6	0.03	0.95	0.84	26.65	TRUE	7.75	4.15	2.44	1.17	Accepted
B02235	3345-7	Animal Farm	4.89E-05	48.9	0.03	0.85	0.85	30.6	TRUE	3.5	3.66	1.63	5.74	Accepted
B02236	3345-7	Animal Farm	4.63E-05	46.3	0.03	0.86	0.85	26.34	TRUE	2.86	5.46	5.62	0.79	Accepted
B02237	3345-4	Animal Farm	2.40E-05	24.0	0.08	0.81	0.6	8.5	FALSE	10.89	10.4	5.31	0.72	Rejected
B02238	3345-4	Animal Farm	2.98E-05	29.8	0.02	0.89	0.58	36.1	TRUE	2.55	3.38	6.69	8.91	Accepted
B02239	3346-10	Animal Farm	3.83E-05	38.3	0.05	0.86	0.76	16.23	TRUE	2.75	6.24	4.92	2.1	Accepted
B02240	3346-10	Animal Farm	3.13E-05	31.3	0.25	0.59	0.43	1.23	FALSE	3.26	17.67	8.12	9.8	Rejected
B02241	3343-7	Animal Farm	2.88E-05	28.8	0.07	0.9	0.89	10.9	TRUE	16.17	7.14	3.87	1.93	Rejected
B02242	3343-7	Animal Farm	2.70E-05	27.0	0.06	0.93	0.93	14.24	TRUE	13.53	8.79	5.36	5.9	Rejected

[a] Notes: int_abs, NRM (A/m); F_{anc}, paleointensity (μT); β, measure of relative data scatter (see text); *f*, NRM fraction (see text); FRAC, NRM fraction by vector difference sum (see text); q, quality factor [Coe et al., 1978]; SCAT, test for scatter of points on Arai plot (see text); DANG, deviation angle (see text); MAD_{free}, free-floating maximum angular deviation (see text); DRAT, average difference of pTRM check normalized by best-fit line (see text); DRATS, cumulative pTRM check difference normalized by pTRM gained at maximum temperature (see text); Status, whether sample was accepted or rejected by selection criteria.

Appendix B: Sample Paleointensity

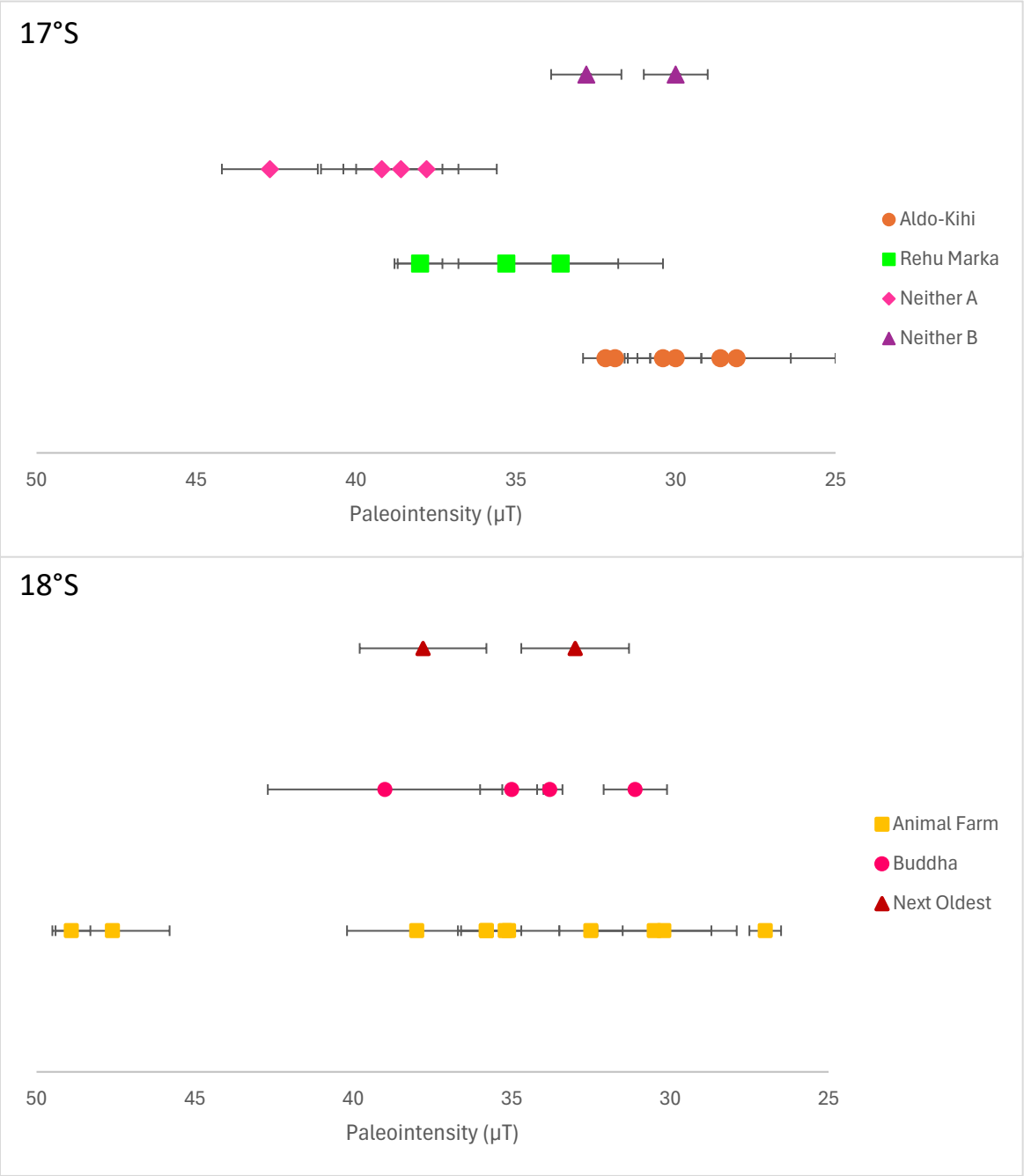

Figure 23: Sample-level paleointensity for flow fields at 17°S and 18°S according to original categorization based on dive observations.

Appendix C: Geochemistry vs Paleointensity-Derived Emplacement Date Estimate

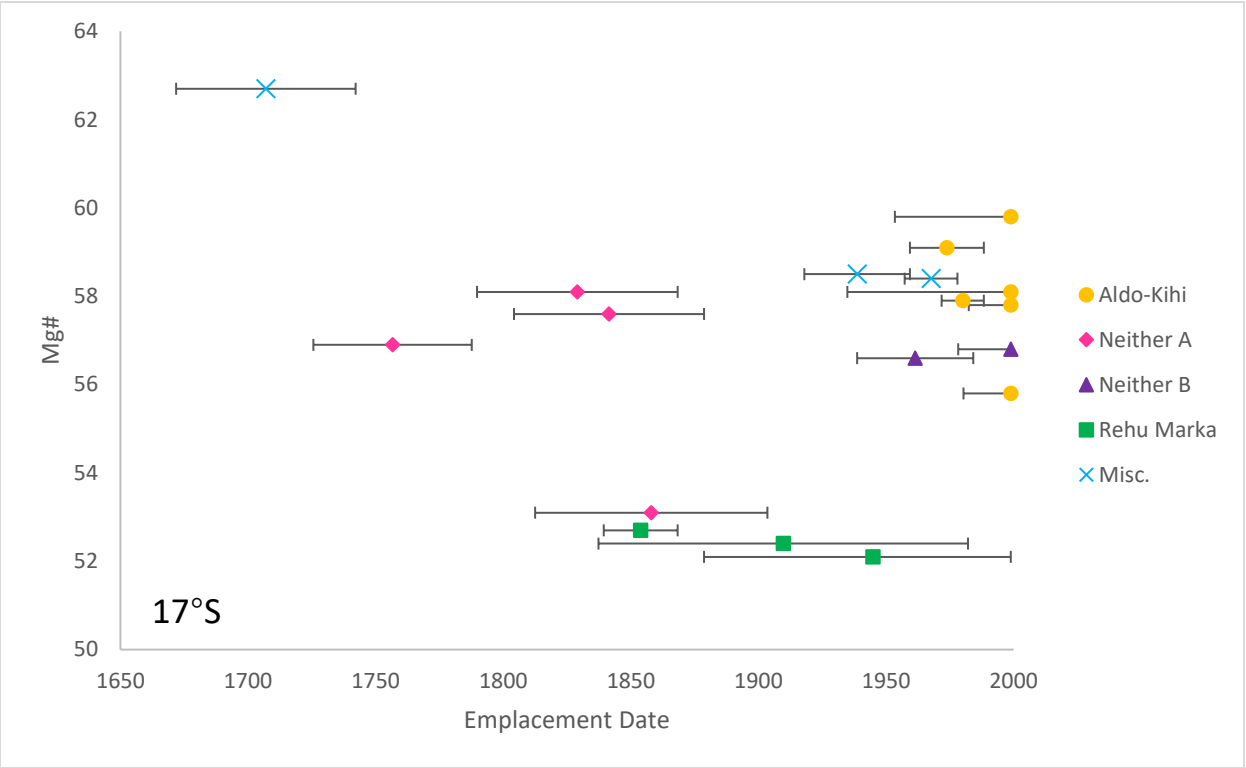

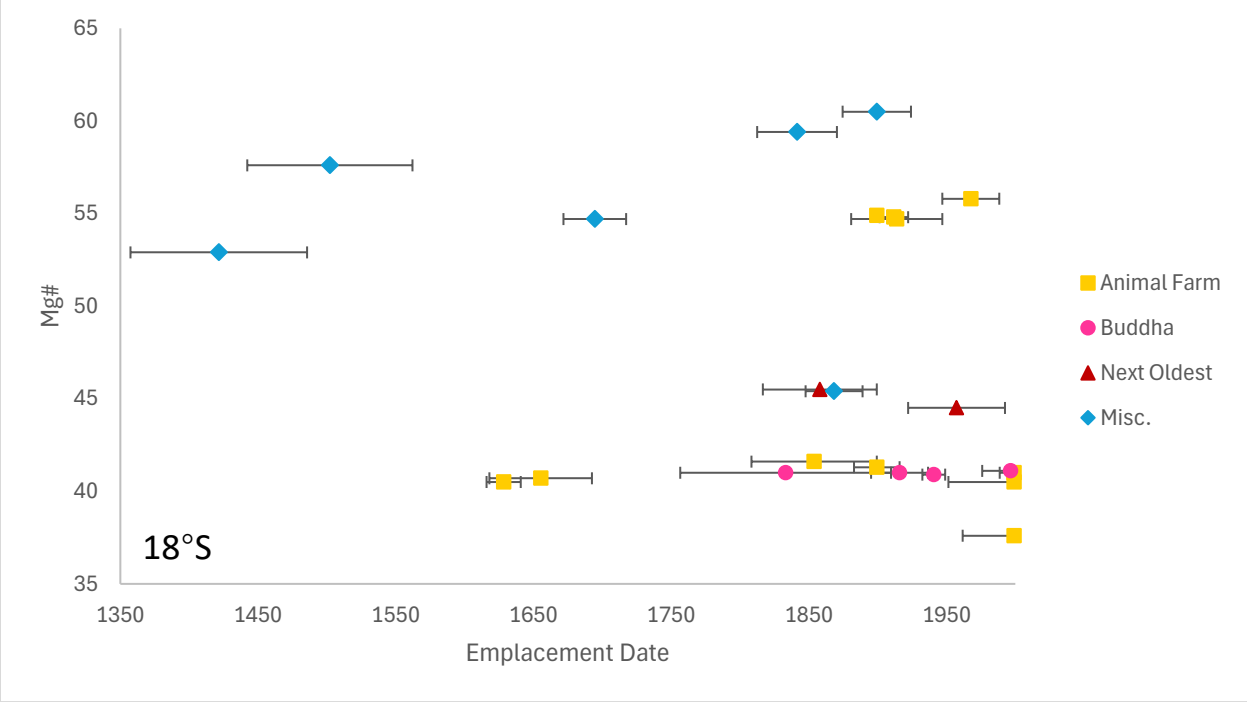

Figure 24: Mg# vs estimated emplacement dates from HFM field model for 17°S and 18°S. Estimated dates after 1999 were set at 1999 as that was the latest possible collection year. Error bars for these dates represent the same estimated age range calculated from the original date but now relative to 1999. Flow field categorization from original categories based on dive observations.

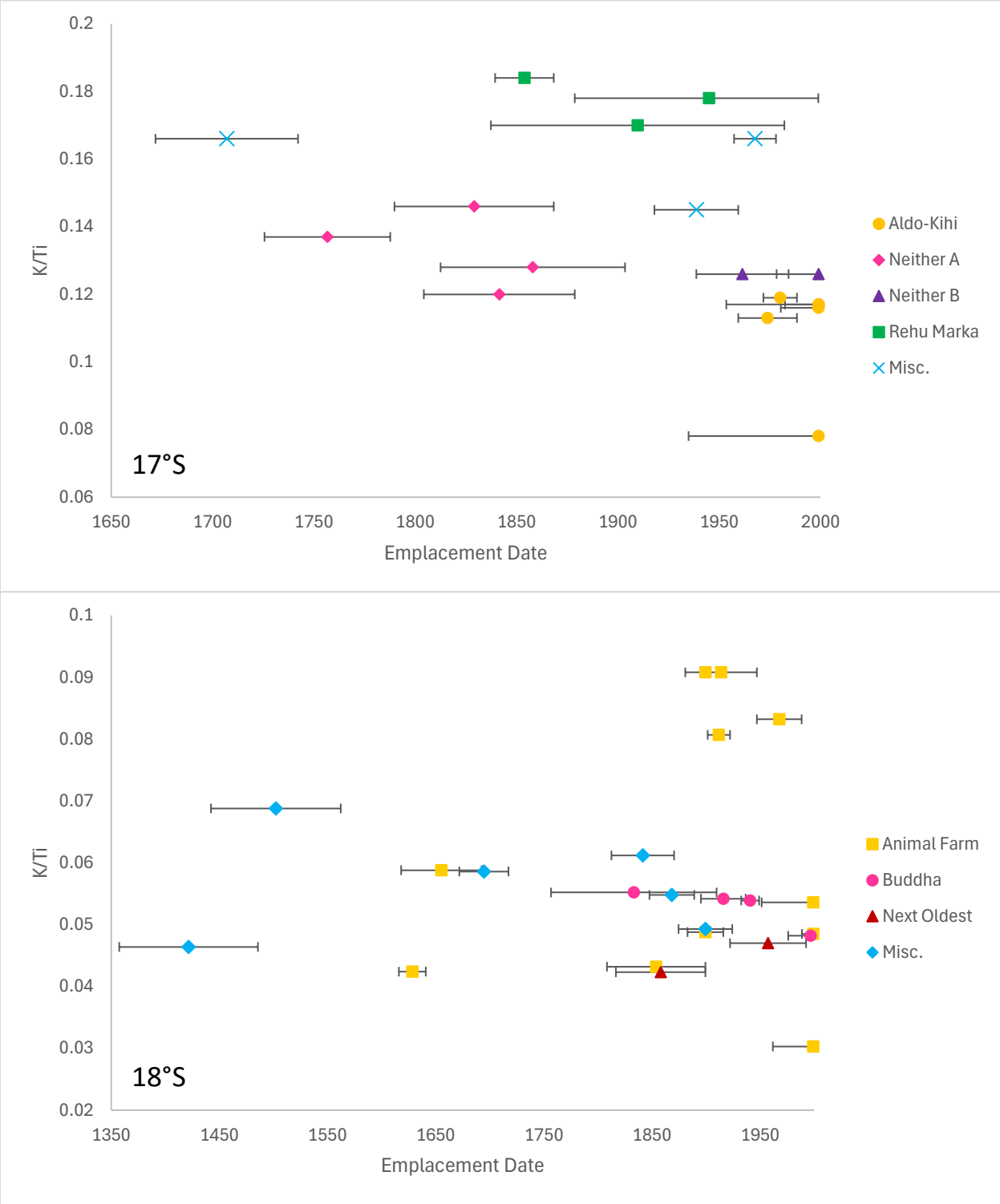

Figure 25: K/Ti vs estimated emplacement dates from HFM field model for 17°S and 18°S. Estimated dates after 1999 were set at 1999 as that was the latest possible collection year. Error bars for these dates represent the same estimated age range calculated from the original date but now relative to 1999. Flow field categorization from original categories based on dive observations.